Supplementary Information:

Internal Conversion of the Anionic GFP Chromophore: In and Out of the I-twisted S_1/S_0 Conical Intersection Seam

Nanna H. List, Chey M. Jones and Todd J. Martínez*

Department of Chemistry and The PULSE Institute, Stanford University, Stanford, CA 94305

SLAC National Accelerator Laboratory, 2575 Sand Hill Road, Menlo Park, CA 94025

*toddjmartinez@gmail.com

Contents

Section S1: Validation of α-CASSCF against XMS-CASPT2

The empirically corrected α-CASSCF[1] method was recently proposed as an efficient and rather accurate approach to describe the photodynamics of $HBDI^-$. In the original work, the α-parameter was fitted for SA2-CASSCF(4,3)/6-31G* on the basis of minimization of the root-mean-square error (RMSE) across all considered critical points. The present work differs in two aspects: i) a three-state averaging is employed to be able to capture the P-twisted conical intersection (MECI-P), and ii) a different parameterization procedure is used in which the α-parameter is fitted to reproduce the vertical excitation energy at the Franck-Condon (FC) geometry, using SA3-XMS-CASPT2(4,3)/6-31G* (frozen core; level shift of 0.3 a.u.; SVP-jkfit density-fitting basis) as reference, and geometries optimized at their respective levels of theory.

Figure S4 shows a comparison of the relative energies of the critical points relevant for the excited-state relaxation in $HBDI^-$ obtained using the fitted α(0.64)-SA3-CASSCF(4,3)/6-31G*. Corresponding energies and key geometric parameters are summarized in Tables S1 and S3-4. This yields a RMSE of 0.30 eV (compared to the original 0.23 eV[1]) across all considered critical points. As seen, α(0.64)-SA3-CASSCF reproduces the relative energetic ordering of the different geometries. Importantly, the relative stability of the I- and P-twisted minima with respect to the FC point is correctly captured. In particular, only MECI-I is accessible from the FC point. Note that correspondingly small active-space CASSCF calculations (i.e., without α-scaling) are inadequate to capture the relative energetics of the FC point and MECIs even qualitatively (Table S1). The twisted geometries are, however, almost uniformly over-stabilized by ~0.3 eV. This leads to energy differences of 0.16 and -0.36 eV with respect to the S_1-planar structure for MECI-P and -I, respectively, as compared to 0.43 and -0.06 eV at the XMS-CASPT2 level. While a larger gradient may accelerate the initial twisting about the ϕ_I and ϕ_P dihedral angles, it is not critical for the present study that focuses on the competition between I- and P-twisted relaxation pathways.

To further validate the adequacy of α-CASSCF for non-adiabatic dynamics simulations, we computed the minimum energy path between the S_1-planar geometry and the I- and P-twisted minima with the nudged elastic band (NEB[2]) method at the α(0.64)-SA3-CASSCF/6-31G* level and compared with energies obtained at the XMS-CASPT2 level along the same path (Figure S5). It should be noted that the S_1-planar geometry is a first-order saddle point (along the I-

torsional coordinate) at the α-CASSCF level rather than a minimum. While it is a true minimum at higher levels of theory, the torsional barriers are of similar, small magnitude. Along the α-CASSCF torsional paths, SA3-XMS-CASPT2(4,3)/6-31G* provides potential barriers of ~0.02-0.03 eV in line with the previously obtained 0.05 eV estimate from relaxed scans at the XMCQDPT2/SA(2)-CASSCF(14,13)/(aug)-cc-pVDZ level.[3]

Geometry optimization, minimum energy conical intersection (MECI) searches and minimum energy pathways (MEPs) were computed using the DL-FIND[4] geometry optimization library and seam MEPs using pyGSM,[5, 6] both interfaced with TeraChem. XMS-CASPT2 calculations were performed using the BAGEL program.[7, 8]

Section S2: Determination of photoproduct quantum yield

To determine the photoproduct quantum yield, the TBFs S_0 which did not couple with other TBFs for at least 5 fs were decoupled and continued independently on S_0 and the resulting stereoisomer distribution was followed for a further 1-ps period. Specifically, TBFs reaching an absolute I-torsion beyond 145° were classified as photoproduct (*E*-isomer), those returning to an absolute I-torsion angle below 55° were classified as ground-state recovery (*Z*-isomer). The remaining were labeled as non-determined. An analogous criterion for the P-torsion was used to classify P-flipping. These angular spans were chosen based on the amplitude of the oscillations around the respective minima following decay to S_0. The photoproduct yields were estimated under the assumption that the isomeric form of the product remained fixed according to its identity after the 150-fs propagation on the ground state. Due to the excess vibrational energy on the hot ground state, there might be some amount of uncharacterized non-statistical isomerization on S_0 that could affect the isomerization yield. Within the 1 ps time span considered, this does however not occur to any significant extent (Figure S11).

Section S3: Analysis of geometric effects with three-state diabatic model

Olsen and McKenzie[9] introduced a three-state-averaged four-electron three-orbital diabatic model based on fragment-localized orbitals to study the effect of the bridge torsional modes on the electronic structure of HBDI⁻. This charge-localized representation was also recently invoked to explain experimentally measured substituent effects on excited-state barriers in Dronpa2 variants.[10] In this paper, we apply the model to analyze the chemical origin of the geometrical

and electronic structures of the intersection seam, in particular focusing of the implications of pyramidalization. For completeness, we briefly revisit the main concepts of this ansatz. For a thorough discussion, the reader is referred to the original paper.[9]

In the three-state diabatic model, the invariance of the energy to orbital transformations within the converged active space is exploited to construct a basis of localized orbitals in which the six singlet configuration state functions (CSFs) can be re-expanded. The CSFs can be divided into covalent and ionic subspaces based on their orbital occupation (Figure S9a). Covalent configurations support one doubly-occupied orbital and two singly-occupied orbitals while the ionic support two doubly-occupied orbitals and one empty (for compactness, spin-adaptation is implicitly assumed in the notation). Importantly, as demonstrated in the original work, Boys localization[11] of the converged SA3-CAS(4,3) active orbitals provides fragment orbitals that are localized on the I- and P-rings as well as on the methine bridge (labeled *i*, *p* and *b*, respectively, in Figure S2b) across a wide range of geometries. Approximate diabatic states are subsequently generated from a unitary block diagonalization[12, 13] between the covalent and ionic configuration subspaces of the resulting configuration interaction Hamiltonian. The three diabatic states dominated by the covalent configurations are labeled as $|X\rangle$, $X = I, P$ or B according to the doubly-occupied fragment orbital. Importantly, in this orthonormalized localized basis, bond formation is a result of mixing between a covalent configuration with its corresponding bond-polarizing ionic configurations.[14] Due to this fragment-localized basis, the exchange integrals and hybrid two-electron integrals are negligible and only the one-electron integrals and the Coulomb repulsion integrals with two electrons in one spatial orbital or two different spatial orbitals contribute significantly. In other words, the interaction between the covalent and ionic configurations, and hence the stabilization of the diabatic states, is governed by the resonance integrals between the relevant fragment-localized orbitals but also by their interaction with the closed-shell electrons.

Here, we use the α-CAS corrected energies in the block diagonalization, recalling that the eigenstates remain unchanged. The Boys localization and construction of the Hamiltonian in the localized basis were performed with MolPro[15, 16] while the α-CAS energy correction was computed with TeraChem and added manually. Figure S9b shows the diabatic state composition at the two twisted S_1 minima as well as the MECIs. To quantify the influence of various

geometrical deformations (pyramidalization, P-torsion and bridge bonds and angle) are shown in Figure S9c.

Effect of bridge pyramidalization and asymmetric bond stretching

Asymmetric bond stretching across the bridge and bridge pyramidalization characteristic of the low-energy regions of the intersection seam act as diabatic-state biasing potentials that preferentially destabilize the torsionally-decoupled diabatic state dominating S_0 (i.e., $|I\rangle$ for MECI-Is) by reducing the contributions from associated bond-polarizing ionic configurations (see Table S6 and Figure S9) and thereby closing the energy gap. This preserves an approximate block-diagonal structure of the effective Hamiltonian (i.e., a two-dimensional $|P\rangle$ and $|B\rangle$ S_1/S_2 block and a one-dimensional block for S_0 for the MECI-Is) characteristic of the I-twisted S_1 minimum and leads to a concomittant de-stabilization of the diabatic $|I\rangle$ state, as required to reach the intersection seam (see diabatic-state composition in Figure S9 and Table S6). Note that this block-diagonal structure is only achieved at out-of-phase configurations where the direction of the HOOP displacement counteracts the rotation of the *b*-orbital relative to the *i*-orbital induced by I-torsion beyond 90° (Figure 6b-d).

Initial force on S_0 after non-adiabatic transition

Without initial kinetic energy, the early dynamics on S_0 immediately following non-adiabatic population transfer will be governed by the direction of steepest descent which involves a shortening of the C_5–C_6 bond and de-pyramidalization at the methine C atom (see schematic in Figure 7a and the gradient difference vector in Figure S7). The initial force on the methine C atom towards planarization (in contrast to an oppositely-directed force on the methine H atom) preserves significant overlap between the *b* and *p* orbitals, thereby increasing the ionic configurations that stabilize the ground state (dominated by the $|I\rangle$ diabatic state) at I-twisted geometries. This driving force results in a rapid, asymmetric contraction of the I-ring and methine bridge planarization.

Section S4: Electron affinities of methyl-truncated I- and P-rings

Vertical electron affinities of the methyl-truncated P- and I-rings were computed using SA3-XMS-CASPT2/6-31G* at the geometries extracted from the S_1-P and the S_1-I minimum, respectively. Specifically, in each case, the structures were truncated after the methine C atom and three H atoms (C–H distance of 1.09Å) were added to saturate the C free valences. Active spaces of (8e,7o) and (8e,6o), comprising all valence π-orbitals, were used for the anionic P- and I-ring systems (with one less active electron for the doublet neutral radicals), respectively. This results in a vertical electron affinity of 1.23 for the P-ring and 0.63 eV for the I-ring. Within the three-state diabatic model, the difference in the electron affinities of the two rings is a result of comparatively larger contributions from stabilizing ionic configurations to the diabatic $|P\rangle$ state at P-twisted geometries relative to the corresponding ionic contributions to the $|I\rangle$ state at I-twisted geometries (Figure S9b).

Section S5: Simple considerations of wavepacket behavior near conical intersections

In general, two limiting regimes may be invoked to describe the wavepacket behavior near intersection seams and the consequent efficiency and outcome of the internal conversion process (Figure S10).[17-21] In the case of ballistic regime, the transfer occurs faster than internal vibrational energy redistribution such that the direction and velocity of approach to the CI (i.e, inertial effects) are the primary parameters governing the dynamics at the seam.[22-24] In the other limit, the time scale of internal conversion is sufficiently slow that near-statistical conditions can be established prior to transfer. Based on simple arguments, we can provide an estimate of the photoproduct quantum yield in the two cases; Ballistic motion along the reactive mode through the CI seam will produce photoproduct (blue dashed arrows). Conversely, in the other regime, the photoproduct distribution becomes statistical, i.e., 1:1 photoproduct/photoreactant (red dashed arrows). Assuming further an equal branching along the two bridge torsions (that is, half the population proceeds along the reactive I-twist pathway, indicated by black arrows), we therefore expect an *E*-isomer quantum yield of about 50% and 25% (of the total population) in the ballistic and statistical regime, respectively.

These two limits can often be roughly correlated with the topography (peaked vs. sloped) of the intersection seam.[20, 21, 25-27] Being local minima on the excited state (stationary points in the (3N-8)-dimensional intersection space and critical points in the full (3N-6)-dimensional

space because of their discontinuous gradient within the branching plane), peaked topographies are canonical photochemical funnels: they are more effective in directing the wavepacket towards the CI seam (i.e., ballistic motion) than their sloped counterparts which lie above a local excited-state minimum. This explains why peaked CIs often feature higher non-adiabatic transfer efficiencies.[19, 28] Moreover, peaked intersections are known for conferring photoreactivity[29-32] because they commonly display two (or more) paths on the ground state (i.e., "bifurcating" CIs[25, 33]). On the other hand, sloped CIs are often single path (i.e., returning to the reactant) and therefore tend to be photochemically non-reactive.[24, 33] For sloped CIs below the FC point, however, excess kinetic energy in the reactive mode may introduce an early non-statistical regime. As further detailed in the main text, $HBDI^-$ represents an intermediate case where early approach to the sloped I-twisted intersection seam is non-statistical along the reactive mode followed by a more statistical behavior.

Section S6: Potential energy scan along I-torsion and HOOP modes

The S_0 and S_1 potential energy surfaces shown in Figure 6a-b were generated as follows. The torsional axis was obtained from a relaxed scan along the I-torsion with the P-torsion constrained at 0°, and therefore, it also includes adjustments of bond distances, angles and bridge pyramidalization. The HOOP axis was obtained from a subsequent unrelaxed scan, starting from the previously determined relaxed structures but with the bridge pyramidalization reset to zero. As shown by the S_1 PES in Figure 6a (black arrow indicates the MEP), this was necessary because of coupling between I-torsion and bridge pyramidalization (most pronounced around ~60° I-twisting).

Section S7: Cone sampling and photoisomerization committor surface

To investigate the impact of potential and inertial effects on photoproduct formation, we compared the outcome of four different schemes initiated at geometries sampled within the branching space of the respective MECI (see below): (i) following the path of steepest descent on S_0, (ii) S_0 dynamics within the NVE ensemble starting with zeroed initial velocities for $HBDI^-$ as well as for a fictitious isotope with an increased mass (15 amu) of the methine H-atom, (iii) S_0 dynamics within the NVE ensemble starting with initial velocities restricted to the branching space with varying amount of initial kinetic energy (ranging from ~0.01 eV corresponding to an

equipartitioning of the energy (~0.44 eV, corresponding to the energy difference between the FC point and MECI-I^+) between all nuclear degrees of freedom, all energy initially associated with the branching plane and an intermediate value. (iv) S_0 dynamics starting with randomized initial velocities following the procedure in the Appendix of Ref. 34. Specifically, atomic velocities were randomly sampled from a Gaussian distribution (with zero mean and unity standard deviation) with subsequent mass-weighting and removal of translation and rotational motion. Finally, a uniform scaling was applied to yield an initial kinetic energy equal to the sum of the kinetic energy of the ground state (2.79 eV within a harmonic approximation) and the energy gap between the FC point and MECI-I^+ (~0.44 eV). A total of 50 random velocity initial conditions were propagated for each geometric displacement and the outcome used to estimate the committor surface for photoisomerization. The committor for each displacement was computed as the fraction of samples that reached the *E*-isomer prior to possibly undergoing non-statistical isomerization on S_0 back to the *Z*-isomer or vice versa (which we did not observe within the 300 fs of S_0 dynamics). In all sampling schemes, geometries were sampled within the branching space of each MECI, as spanned by its characteristic gradient difference and derivative coupling vectors (defined according to Yarkony's procedure[35] and imposing that $\Delta_{gh} \geq 0$ and $\theta_s \in \left[0, \frac{\pi}{2}\right]$ [33]). The polar angle (0-360°) was discretized in 18 steps and the radial coordinate were sampled between 0.005 and 0.02 a.u. in four steps (additional 0.025 and 0.03 a.u. were included for the S_0 minimum energy paths). In the case of (i), the original Z-isomer was recovered upon steepest descent from all (MECI-I^+, MECI-$I2^+$ and the approximate transition state on the connecting seam) whereas the *E*-isomer was produced for the conical intersection resembling MECI-I^+ but with oppositely directed P-torsional angle. The ground state dynamics was performed at the same electronic-structure level of theory as the AIMS simulations (see main text).

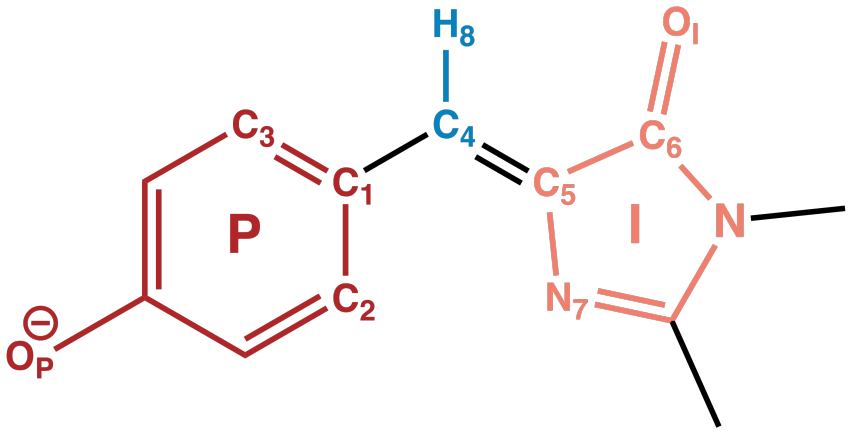

Definition of key geometric parameters

$$\theta_{\text{pyr}} = \arccos\left((\mathbf{e}_{C_1\text{-}C_4} \times \mathbf{e}_{C_5\text{-}C_4}) \cdot \mathbf{e}_{H_8\text{-}C_4}\right) - \frac{\pi}{2}$$

$$\phi_I = \text{sgn}_I \cdot \arccos\left((\mathbf{e}_{C_1\text{-}C_4} \times \mathbf{e}_{C_5\text{-}C_4}) \cdot (\mathbf{e}_{C_5\text{-}C_4} \times \mathbf{e}_{C_6\text{-}N_7})\right)$$

$$\text{sgn}_I = \text{sgn}\left(((\mathbf{e}_{C_1\text{-}C_4} \times \mathbf{e}_{C_5\text{-}C_4}) \times (\mathbf{e}_{C_5\text{-}C_4} \times \mathbf{e}_{C_6\text{-}N_7})) \cdot \mathbf{e}_{C_5\text{-}C_4}\right)$$

$$\phi_P = \text{sgn}_P \cdot \arccos\left((\mathbf{e}_{C_5\text{-}C_4} \times \mathbf{e}_{C_1\text{-}C_4}) \cdot (\mathbf{e}_{C_1\text{-}C_4} \times \mathbf{e}_{C_3\text{-}C_2})\right)$$

$$\text{sgn}_P = \text{sgn}\left(((\mathbf{e}_{C_5\text{-}C_4} \times \mathbf{e}_{C_1\text{-}C_4}) \times (\mathbf{e}_{C_1\text{-}C_4} \times \mathbf{e}_{C_3\text{-}C_2})) \cdot \mathbf{e}_{C_1\text{-}C_4}\right)$$

Figure S1. Definition of pyramidalization and dihedral angles. Here, $\mathbf{e}_{\text{Y–X}}$ denotes a unit vector pointing along the bond from atom X to atom Y. Sign factors are given by the projection of the cross product of the normal vectors along the central bond. Using this definition of the handedness of bridge dihedrals, conrotatory motion corresponds to $(\phi_{\text{P}},\phi_{\text{I}}) = (\pm,\mp)$ and disrotatory to $(\phi_{\text{P}},\phi_{\text{I}}) = (\pm,\pm)$, see also Figure S6. With this definition of the pyramidalization angle, an idealized sp^2 C atom would give a 0° while an idealized sp^3 C atom, as in methane, corresponds to 55°.

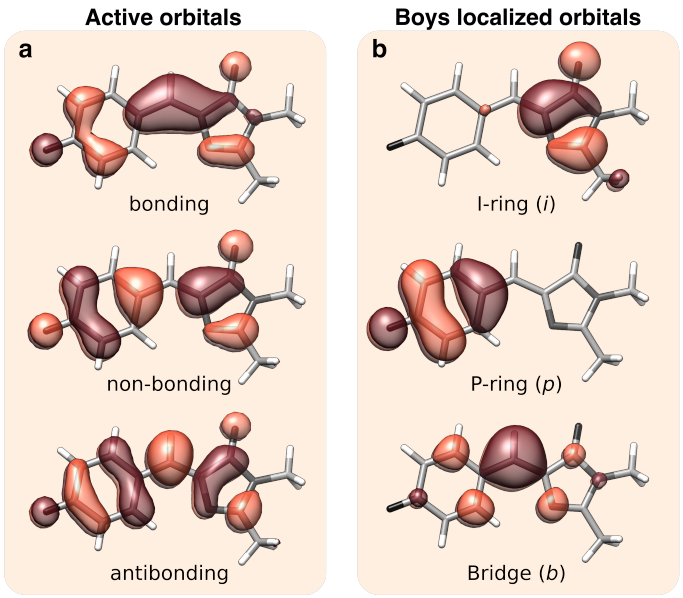

Figure S2. Active-space orbitals. (a) The three orbitals constituting the active space for the SA3-α(0.64)-CASSCF and SA3-XMS-CASPT2 calculations, given at the FC geometry. (b) Localized fragment orbitals on the I-ring (*i*), P-ring (*p*) and bridge (*b*) fragments as obtained by Boys localization. Isovalue: 0.03 a.u.

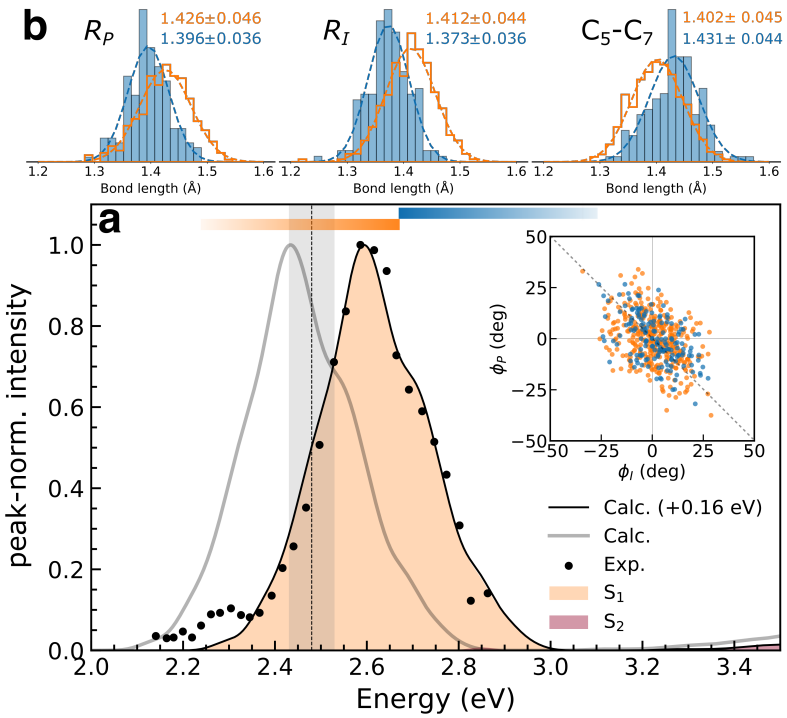

Figure S3. Initial condition sampling. (a) Comparison of simulated and experimental electronic absorption spectrum of $HBDI^-$ computed based on 500 configurations sampled from a finite-temperature (300 K) ground-state harmonic Wigner distribution (excluding three modes dominated by linearized methyl rotations) computed at the MP2/cc-pVDZ level of theory. Individual sticks were convolved with a Gaussian envelope (FWHM=0.07 eV) and shifted +0.16 eV to align with the experimental absorption maximum (2.59 eV with a 45 nm FWHM[36]). The gray area marks the energetic window within which the initial conditions for the AIMS dynamics were selected (pump photon energy 2.48±0.05 eV).[37, 38] As shown in previous work,[39] the shoulder on the blue side (above ~2.7 eV) of the absorption band arises from excitations of a vibrational mode dominated by an in-phase stretching of the bridge bonds while out-of-phase relative to the C_5-N_7 bond (see Figure S1 for atom numbering and definitions of key geometric parameters). The experimental spectrum was digitized from Ref. 36. The inset shows the conrotatory dihedral distribution from the ground-state sampling. (b) Distributions of bond distances for the (i) C_1-C_4, (ii) C_4-C_5 and (iii) C_5-N_7 bonds for sampled geometries with excitation energies below and above 2.66 eV (orange and blue, respectively). Numbers correspond to the mean bond lengths and standard deviations (Å).

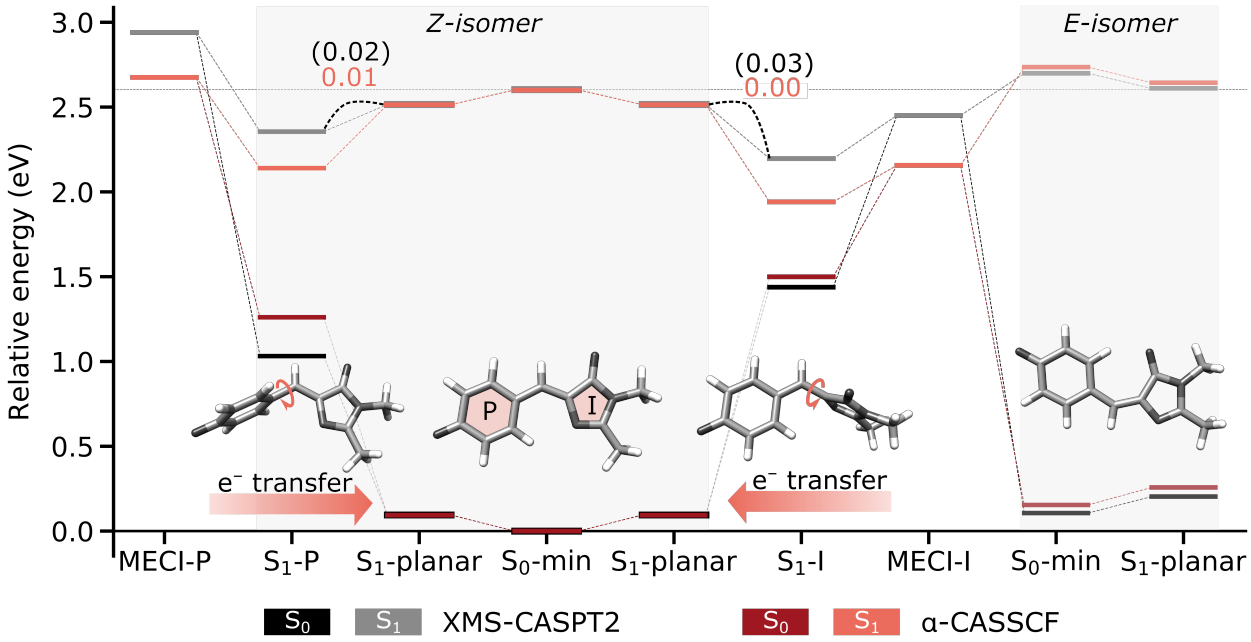

Figure S4. Comparison of S_0 and S_1 potential energies for $HBDI^-$ at important geometries obtained using SA3-α(0.64)-CASSCF(4,3)/6-31G* (red shades) and SA3-XMS-CASPT2/6-31G* (gray shades) at their respective levels of theory (tabulated energies provided in Table S1). The α-parameter was determined by fitting to reproduce the vertical excitation energy at the FC geometry (α-CASSCF overlaps the XMS-CASPT2 at planar geometries). While α-CASSCF tends to over-stabilize twisted structures relative to planar structures, it correctly reproduces the relative ordering and that MECI-$P^{+/-}$ lies above the FC point, while MECI-$I^{+/-}$ lies below (the superscript indicating isoenergetic enantiomers has been left out). Note that S_1-planar is not a true minimum at the α-CASSCF level of theory. The torsional barriers (eV) are shown above the curved dashed lines.

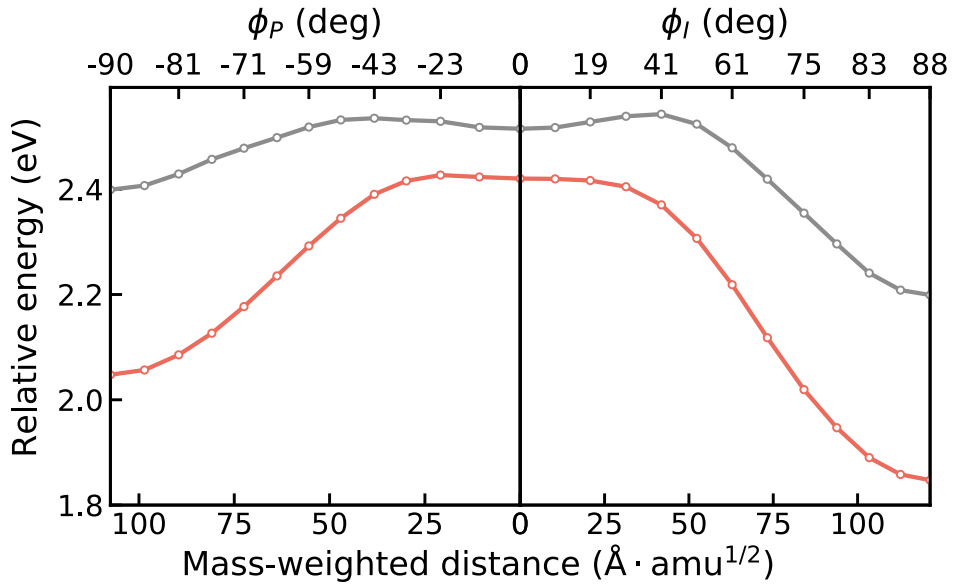

Figure S5. Relative energies along the S_1 minimum energy path connecting the S_1-planar to each of the two twisted minima (left: S_1-P, right: S_1-I) as obtained using the nudged-elastic-band method[40] and α(0.64)-CASSCF(4,3)/6-31G* (orange line). The gray line shows the corresponding XMS-CASPT2(4,3)/6-31G* relative energies computed at the same geometries. The reduced barriers and larger downhill gradients will contribute to faster deplanarization in the α-CASSCF nonadiabatic dynamics. Note that the S_1-planar geometry is not a true minimum at the α(0.64)-CASSCF(4,3)/6-31G* level of theory.

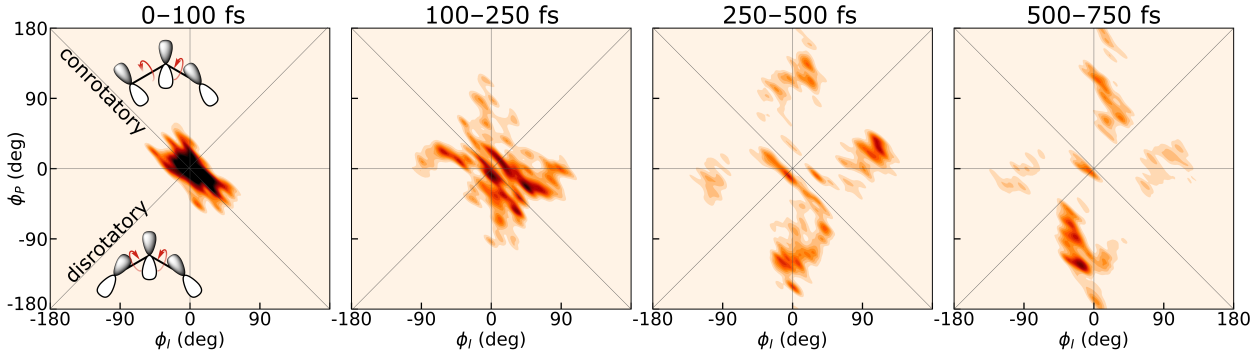

Figure S6 Early time evolution of the S_1 wavepacket density along the bridge-torsional modes, averaged over the specified time intervals. The reduced densities were computed using a previously-described Monte Carlo procedure.[41] The departure from the FC point proceeds along one-bond-flip dominated pathways with an imprint of the initial conrotatory distribution of dihedral angles (see Figures S1 and S3). The non-visited disrotatory pathways would dynamically correspond to a hula-twist motion.

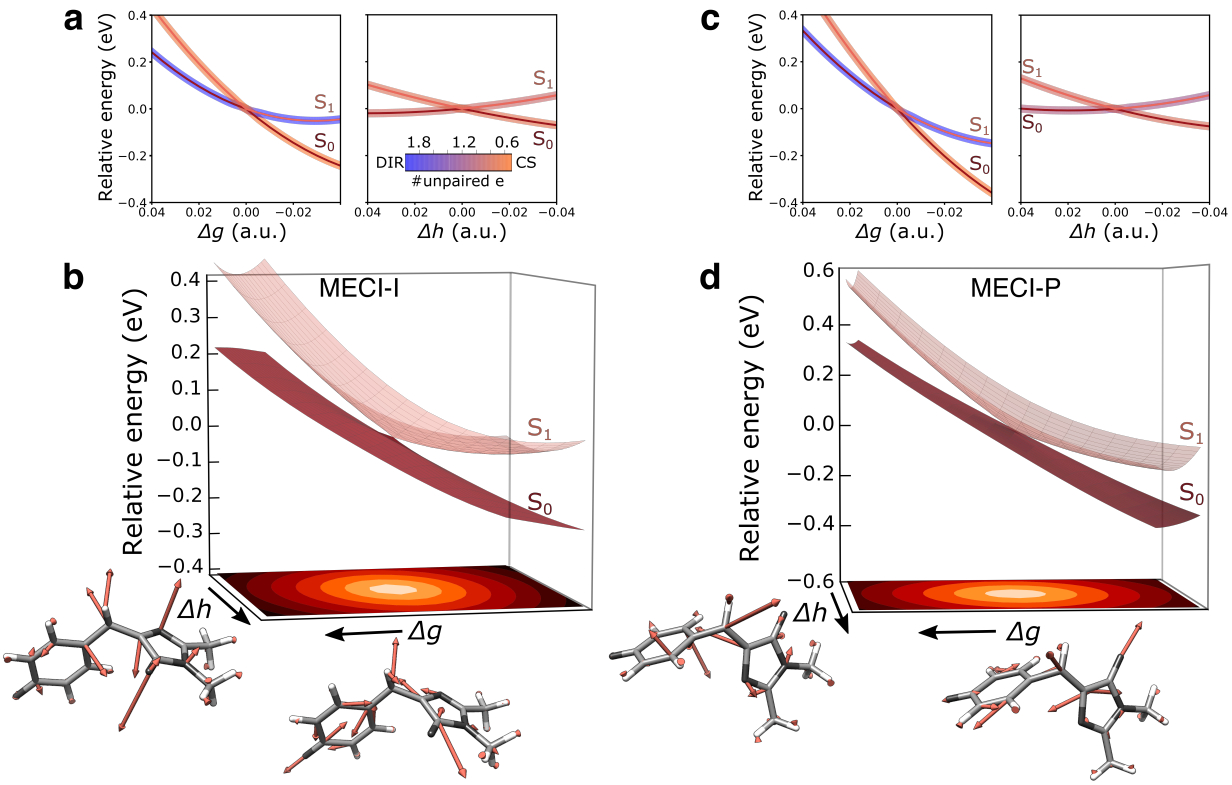

Figure S7. Local topographies of the MECIs of HBDI$^-$. (a) S_1 and S_0 potential energy cuts for MECI-I$^+$ along the direction of the g- and h-vectors[35] with line shading indicating the electronic character of the adiabatic state in terms of effective number of unpaired electrons:[42] a value close to two indicates a diradical (DIR) character which is shaded in blue, while a value close to zero indicates the closed-shell (CS) charge-transfer electronic configuration shaded in orange. The electronic character switches from DIR to CS along the direction of the gradient-difference vector for both MECIs. (b) Cone plot for MECI-I$^+$ for displacements of ±0.04 Å. (c) and (d) are the corresponding plots for MECI-P$^+$. S_1 and S_0 energies are reported with respect to that of the respective MECI and the energy gap is shown as a contour plot. Intersection parameters, as defined in Ref. 33, are provided in Table S5. Both MECIs are sloped in the direction of the gradient vector while peaked along the non-adiabatic coupling vector. The arrows on the molecules represent unit vectors along the +g- and +h-directions (ranges extend from ±0.04 a.u. where black arrows indicate positive displacement direction). For both MECIs, the gradient difference corresponds to a combination of bond-length alternation and HOOP motion, while the non-adiabatic coupling vector is dominated a linearized torsional motion along ϕ_I. The g-vector corresponds roughly to the direction of approach to the MECIs.

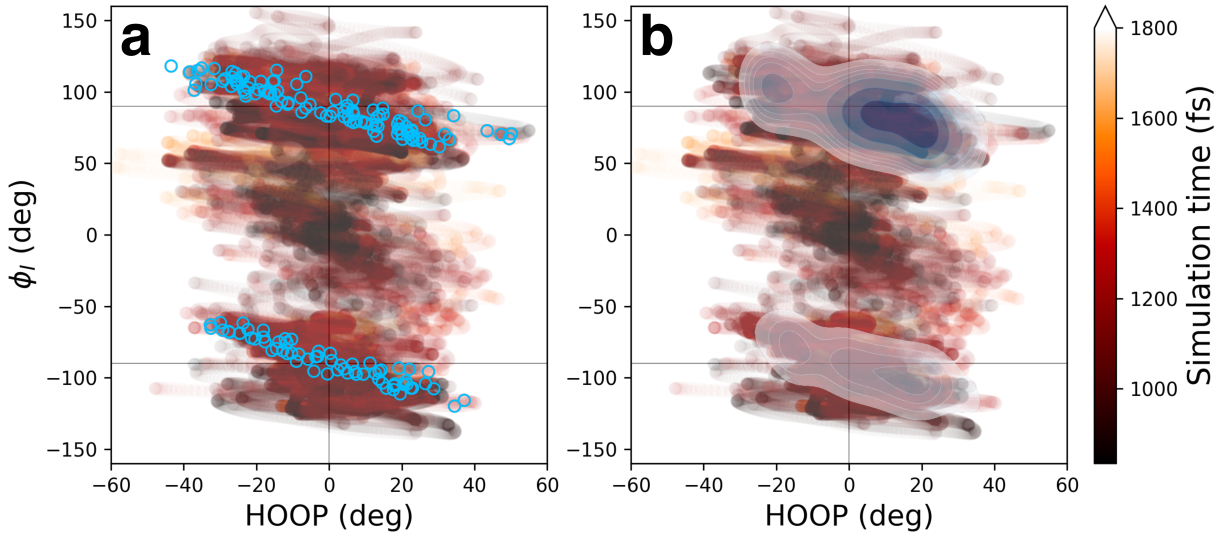

Figure S8. Time evolution (see color code) of the centroids of the trajectory basis functions in the subspace spanned by the HOOP and I-torsional modes. The faster HOOP mode initially follows the rotation direction of the I-dihedral, while the distribution is wider and centered around 0° when the I-torsion reaches ~90°. (a) As indicated by the blue open circles, the non-adiabatic transition events occur at out-of-phase configurations (Figure 6). (b) The blue contours show the associated absolute population transfer (i.e., each spawn is weighted by the population transferred and convolved with a Gaussian function) and highlights the bimodal distribution. The somewhat asymmetric spawning distributions relative to direction of the I-torsion is likely a consequence of the relatively small number of initial conditions used in this work since the underlying potential energy profile is symmetric.

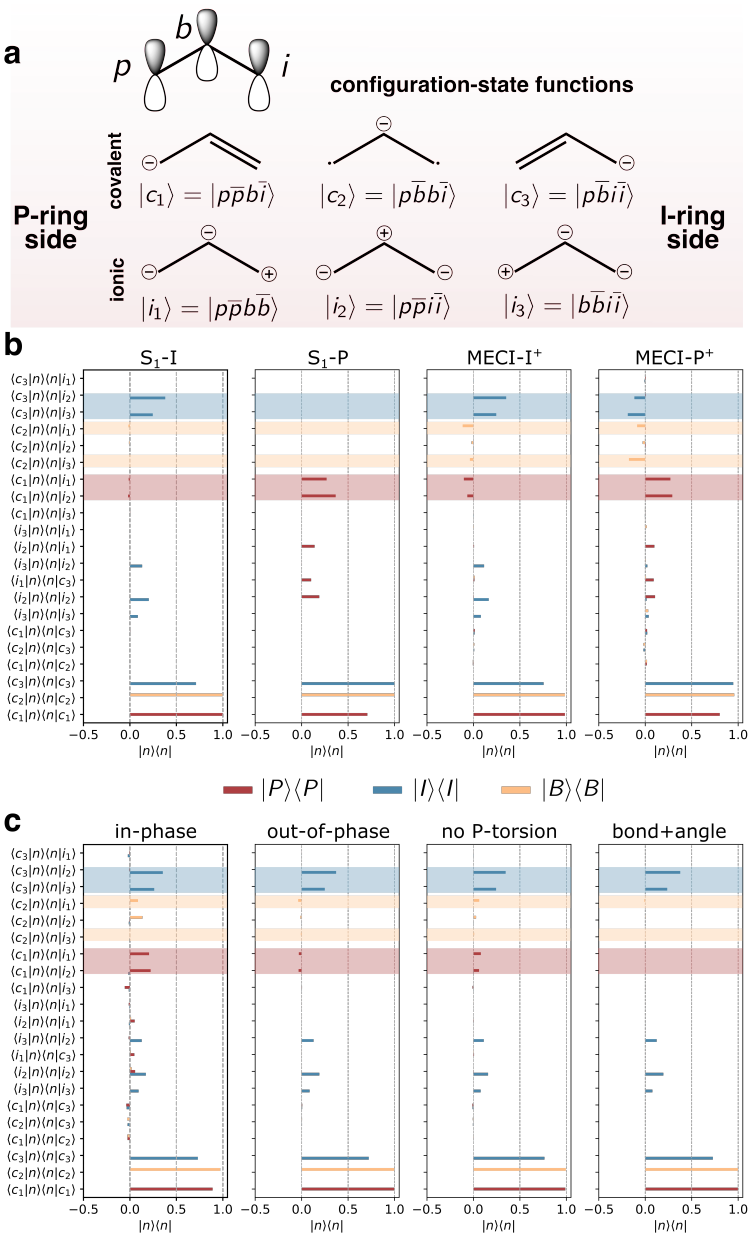

Figure S9. Geometric effects on diabatic-state composition. (a) Schematic of the three fragment-localized orbitals (see also Figure S2) together with the singlet CSFs that can be generated by distributing four electrons in these three orbitals. For compactness, spin-adaptation is implicitly assumed in the notation. The covalent configurations support one doubly-occupied and two singly-occupied orbitals while the ionic configurations correspond to two doubly-occupied orbitals. (b-c) Decomposition of the diabatic states in terms of the underlying CSFs, see (a). Within this orthonormalized fragment-localized basis, bond formation is a consequence of coupling between the leading covalent configuration (to a given diabatic state) and its corresponding bond-polarizing ionic configurations. The color-coding indicates diabatic states, and the same-colored shaded areas highlights the bond-stabilizing ionic contributions for each diabatic state. (b) at twisted S_1 minima and MECIs; (c) at the selected distorted geometries in Table S6.

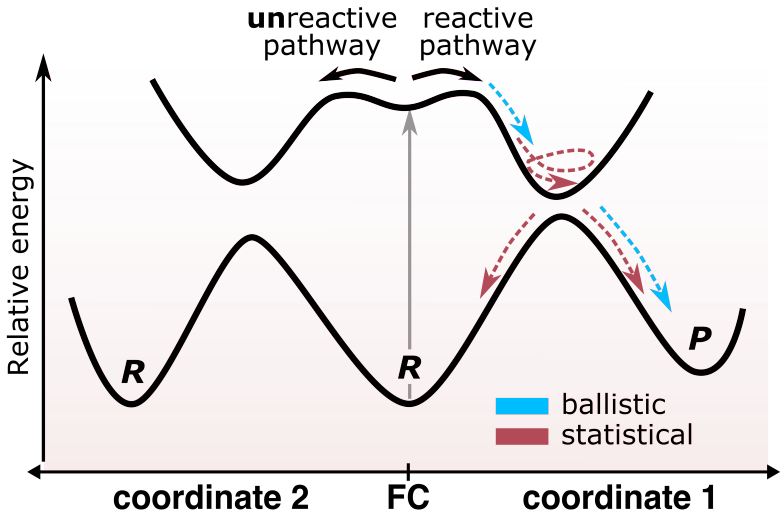

Figure S10. Schematic of the two limiting regimes of wavepacket behavior near a conical intersection (blue arrows: ballistic, red arrows: statistical) showing their impact on photoproduct quantum yield (*R*: photoreactant; *P*: photoproduct). While the potential energy curves resemble those of $HBDI^-$, i.e., with two competing pathways (one reactive and one unreactive), the dashed arrows are only intended to illustrate behavior in two limiting regimes. In the idealized case, the ballistic regime only produces the photoproduct, while the statistical regime leads to equal fraction of photoreactant and -product.

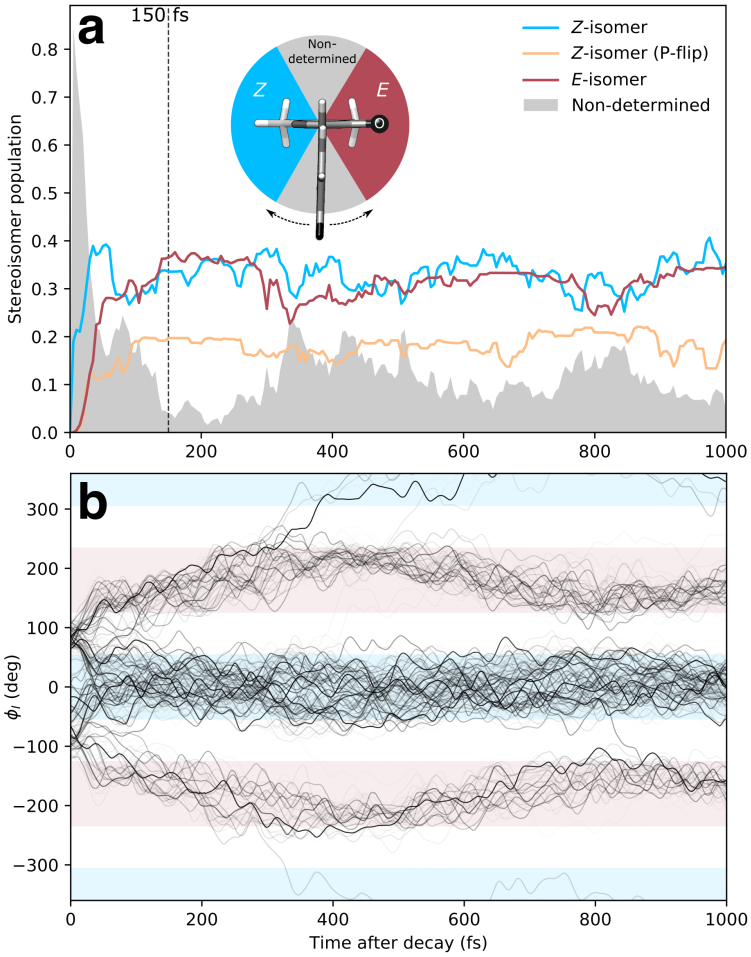

Figure S11 (a) Time evolution of the stereoisomer distribution of photoproducts after decay to S_0 relative to the total population. Time zero corresponds to the spawning entry point for each TBFs, i.e., they have been temporally realigned. The inset figure illustrates the stereoisomer classification used for I-twisting (±55° relative to the respective ground-state minimum). Similar criterion was used for P-twisting although the isomers are identical due to the symmetry of the P-ring in $HBDI^-$. (b) Evolution of the I-dihedral for each spawned TBF on S_0 (lines). The transparency of the lines indicates the absolute population of the given TBF. The blue- and red-colored shadings follow the classification for photoreactant and -product in (a). The majority of TBFs oscillate around *Z/E*-isomer ground-state valleys within 1 ps and only a few escapes to undergo further rotation.

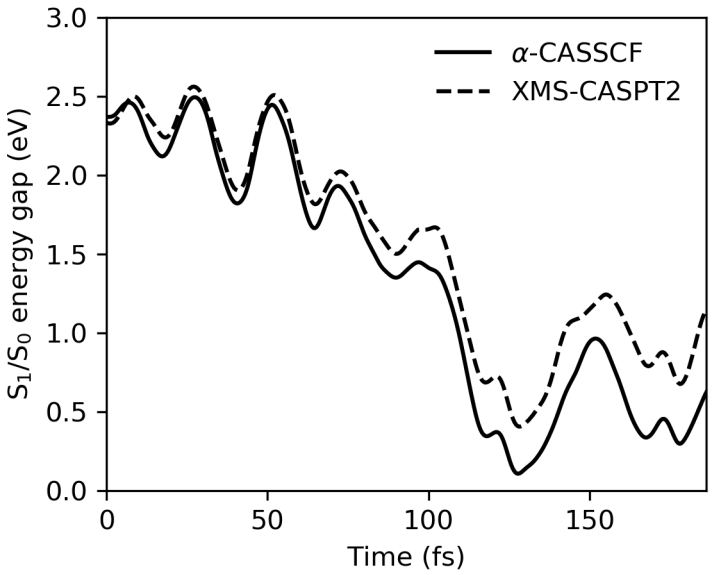

Figure S12 Comparison of the S_1/S_0 energy gaps for $HBDI^-$ along a representative TBF on S_1 progressing along the I-twist pathway obtained using SA3-α(0.64)-CASSCF(4,3)/6-31G* (solid) and SA3-XMS-CASPT2/6-31G* (dashed). The behavior of α-CASSCF at distorted geometries is consistent with the results reported for critical points (Figure S4), with a tendency to over-stabilize twisted structures.

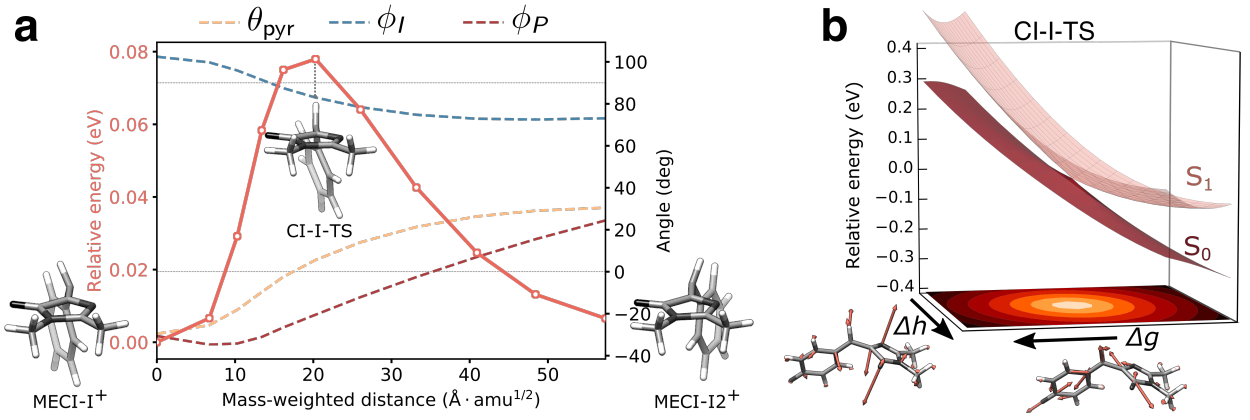

Figure S13. (a) Seam minimum energy path (solid line, left y-axis) connecting MECI-I^+ and MECI-$I2^+$ with bridge torsion and pyramidalization indicated (dashed lines, right y-axis). The approximate transition state (CI-I-TS) on the I-twisted intersection seam is characterized by a nearly planar methine bridge. (b) Cone plot of CI-I-TS for displacements of ±0.04 Å along each of the branching vectors. S_1 and S_0 energies are reported with respect to the CI and the energy gap is shown as a contour plot. The intersection parameters for the two MECI-Is and CI-I-TS are provided in Table S5. Following minimum energy paths on the ground state starting from structures sampled in proximity of each of the MECI-Is as well as at CI-I-TS lead to recovery of the original *Z*-isomer.

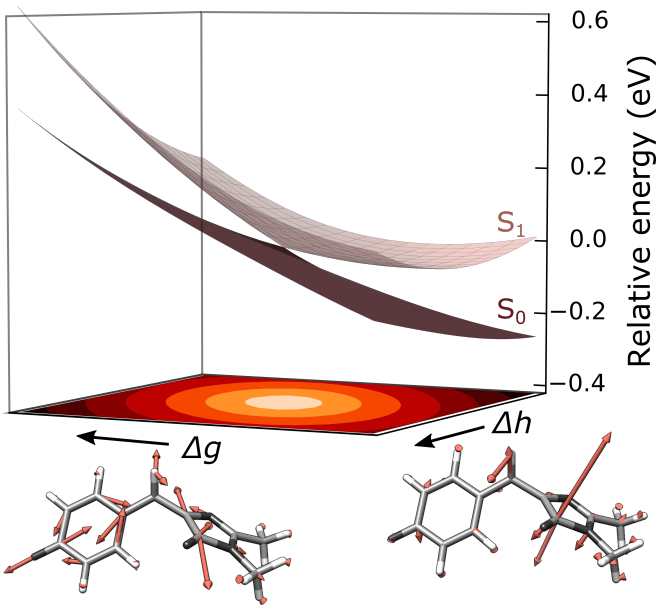

Figure S14. Local topography of a conical intersection (labeled CI-I$^+$-P) on the I-twisted intersection seam, similar to MECI-I+ but with the P-dihedral angle rotated oppositely of the pyramidalization direction. Cone plot was generated for displacements of ±0.04 Å and the black arrows indicates positive displacement direction. S_1 and S_0 energies are reported with respect to the CI and the energy gap is shown as a contour plot. Intersection parameters, as defined in Ref. 33, are provided in Table S5. Following the S_0 minimum energy path starting in the vicinity of this part of the seam space leads to formation of the *E*-isomer.

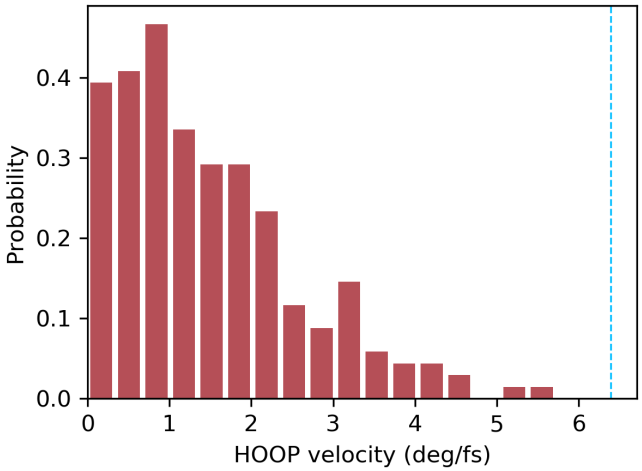

Figure S15. Distribution of HOOP velocities at non-adiabatic transition events. The blue dashed line indicates the maximum HOOP velocity attained by the I-twisted S_1 population. The majority of the transfer occurs at comparatively low velocities, consistent with the low-energy part of the I-twisted CI seam being reached upon large displacements along the HOOP mode.

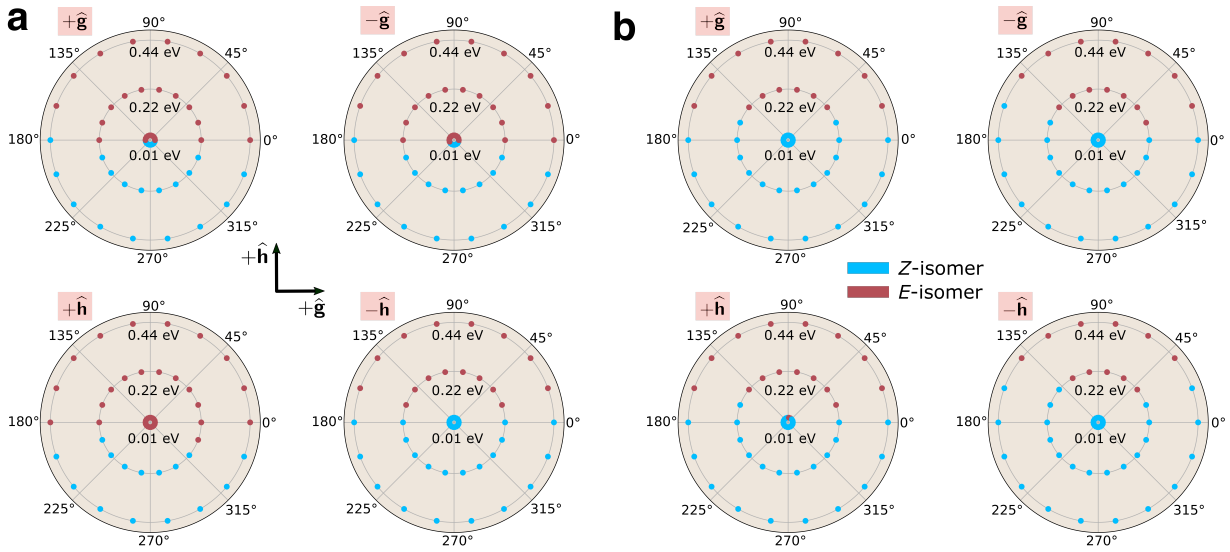

Figure S16. Implications of inertial effects within the branching space on photoproduct generation from the I-twisted intersection seam for (a) MECI-I$^+$ and (b) MECI-I2$^+$. As indicated by the associated red-shaded box, each polar plot represents a specific displacement along the g- and h-directions (at a radius of 0.02 a.u.). The polar angle of each point indicates the direction of the initial velocities within the branching space while the radius specifies the initial kinetic energies (marked by the numbers in the plots). Note that this is different from the polar plots in Figures 7 and S17 where the points represent geometric displacements (rather than velocity direction) within the branching plane. Three different kinetic energies were investigated corresponding to: equipartitioning of the energy (~0.44 eV, corresponding to the energy difference between the FC point and MECI-I$^+$) between all nuclear degrees of freedom, all energy initially associated with the branching plane and an intermediate value.

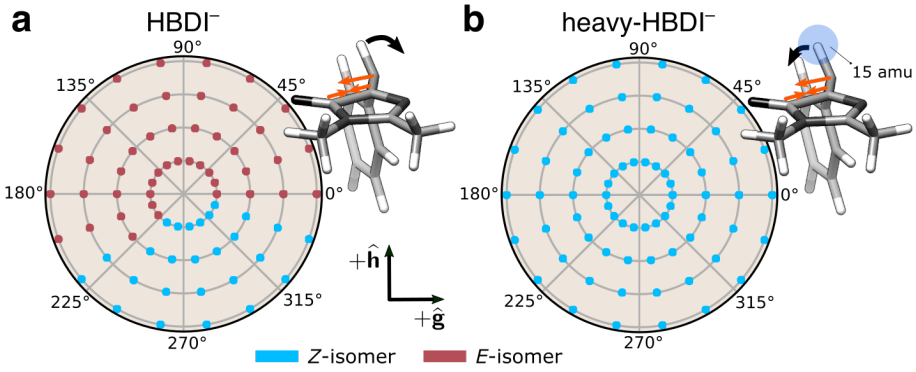

Figure S17. Implications of inertial effects gained on S_0 in the vicinity of MECI-I$^+$ for photoproduct generation. Comparison of the photoproduct distribution at each displacement within the branching plane as obtained from S_0 dynamics starting with zeroed initial velocities for (a) unmodified HBDI$^-$ and (b) with an artificially heavy methine H-atom (~15 amu). For HBDI$^-$, the contraction of the I-ring and planarization of the methine bridge accelerates the light methine H-atom in the direction of photoproduct generation (see orange and black arrows). For geometries slightly displaced along the h-direction, this is sufficient to overcome the ridge on the ground state (see Figure 6b) and produce the *E*-isomer. On the other hand, the heavier methine H-atom in (b) slows down the HOOP motion to a time scale closer to that of the I-torsional motion. This impedes ridge crossing and hence photoproduct formation. We note that a recent study by Conyard *et al.* investigated the effect of bridge methylation and found that this accelerated

non-radiative decay.[43] However, the resulting steric crowding introduces non-negligible effects on the potential energy surface. On the other hand, introducing a fictitious heavy hydrogen allows us to investigate purely inertial effects by specifically lowering the momentum gain along the HOOP coordinate on S_0 and diminishing the effective mass difference between the HOOP and torsional degrees of freedom.

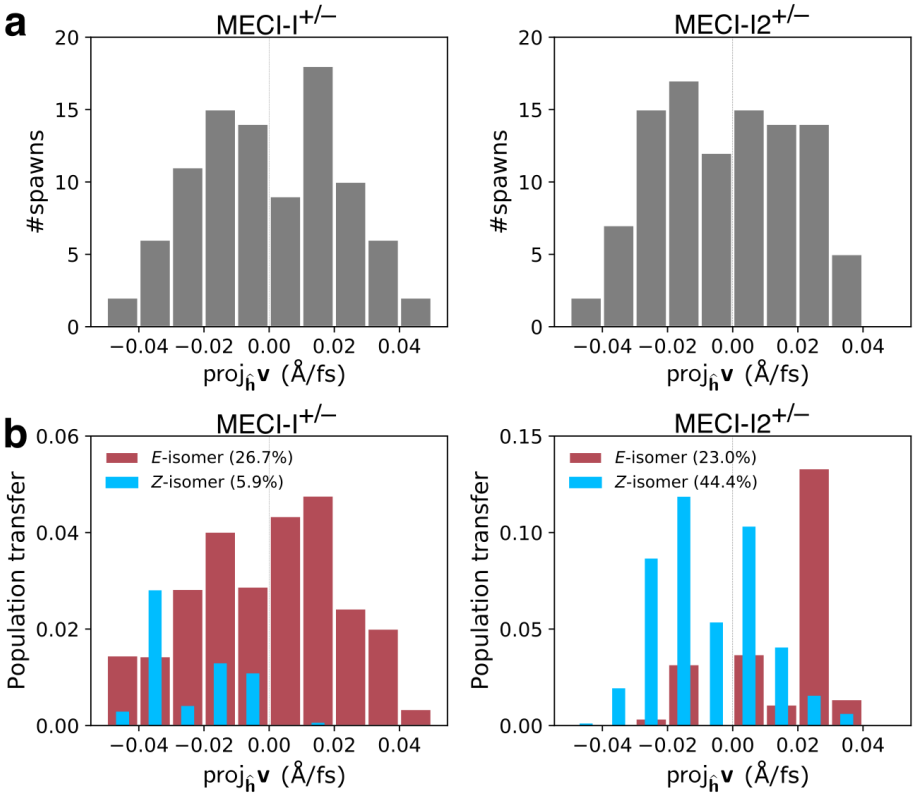

Figure S18. Distributions of the velocity components for the parent TBFs along the +h-direction at the non-adiabatic transition events as categorized by MECI-I type. Events for both positive and negative ϕ_I directions have been combined. (a) Based on number of non-adiabatic transition events. In both cases, the distribution is close to symmetric about zero. (b) Weighted by the population transfer relative to the total I-twisted S_1 population and categorized according to outcome of the ensuing S_0 dynamics. Note the different ranges on the y-axes. The spiked *E*-isomer formation for MECI-I2$^{+/-}$ originates predominantly from the initial approach to the intersection seam.

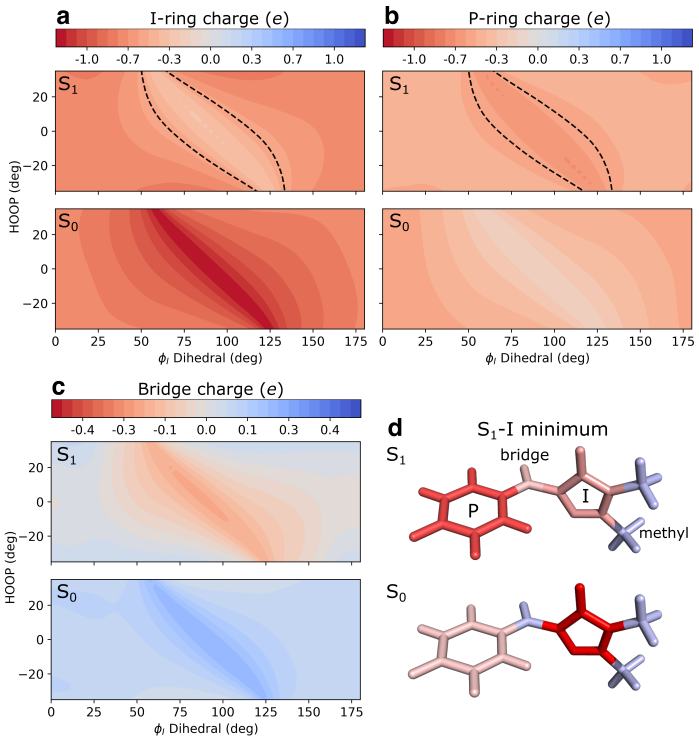

Figure S19. Charge redistribution along the I torsional and HOOP mode. Mulliken charges for the S_1 and S_0 states accumulated for the (a) I-ring, (b) P-ring and (c) methine bridge, see also (d). Note the smaller charge range used in (c). The dashed black line separates regions of opposing charge-transfer polarity, i.e., geometries enclosed by the lines are characterized by electronic charge accumulation on the P-ring relative to the I-ring in the S_1 state. As evident, the out-of-phase geometries largely preserve the electronic charge redistribution from the S_1-I minimum, and that a change in the HOOP direction is enough to revert the polarity across the two rings. In other words, HOOP motion separates region of distinct polarity. As detailed in the main text and shown in Figure 4d, this is a result of the HOOP counteracting the electronic coupling between the *b* and *i* orbitals otherwise introduced by displacement along the I-torsion. In other words, the out-of-phase geometries retain the approximate block-diagonal form of the Hamiltonian in the diabatic basis with a two-dimensional block (S_1/S_2) and a one-dimensional block (S_0). (d) Accumulated charges at the S_1-I minimum, indicating the atoms defining each charge group. The charges were computed at the α(0.64)-CASSCF(4,3)/6-31G* level of theory.

Table S1. SA3-α(0.64)-CASSCF(4,3)/6-31G* and SA3-XMS-CASPT2(4,3)/6-31G* energies (eV) for critical points of $HBDI^-$ optimized at their respective level of theory. Energies are reported relative to the ground state energy at the corresponding FC point. The corresponding energies for SA3-α(0.64)-CASSCF(4,3)/6-31G* shows that the a-scaling is essential to capture the energetic ordering of the FC point and the MECIs.

	S_0 (*Z*)	S_1-planar (*Z*)	S_1-I	S_1-P	MECI-I^+	MECI-$I2^+$	MECI-P^+	S_0 (*E*)	S_1-planar (*E*)
					α-CASSCF				
S_0	0.000	0.094	1.499	1.260	2.156	2.163	2.675	0.154	0.257
S_1	2.600	2.514[a]	1.941	2.140	2.156	2.163	2.675	2.736	2.644
S_2	3.795	3.702	4.575	4.956	4.482	4.556	4.685	3.969	3.881
					XMS-CASPT2				
S_0	0.000	0.095	1.438	1.032	2.451	2.478	2.940	0.106	0.204
S_1	2.603	2.514	2.196	2.355	2.451	2.478	2.940	2.699	2.610
S_2	3.807	3.683	4.740	5.325	4.724	4.787	5.189	3.974	3.843
					CASSCF[b]				
S_0	0.000	0.162	2.039	1.602	2.919	2.913	3.497	0.154	0.330
S_1	4.063	3.944	2.729	2.976	2.919	2.913	3.497	4.188	4.058
S_2	5.930	5.800	6.845	7.376	6.554	6.652	6.638	6.115	5.991

[a] A first-order saddle point on S_1 rather than a minimum (see Figures S4-S5).
[b] Evaluated at the geometries optimized at the α-CASSCF level.

Table S2. Mulliken charges at important geometries for the ground and first excited state of $HBDI^-$ obtained at the α(0.64)-SA3-CASSCF(4,3)/6-31G* level of theory. The fragments used for charge accumulation are shown in Figure S19d, given at the S_1-I minimum. Coupling between torsional motion and charge redistribution is exemplified along the I-torsion in Figure S19.

	S_0-min		S_1-planar		S_1-I		S_1-P	
	S_0	S_1	S_0	S_1	S_0	S_1	S_0	S_1
I-ring	-0.743	-0.708	-0.740	-0.729	-1.257	-0.342	-0.390	-0.857
P-ring	-0.556	-0.484	-0.582	-0.497	-0.200	-0.691	-0.989	-0.054
Bridge	0.066	-0.033	0.081	-0.008	0.229	-0.209	0.158	-0.296
Methyl	0.233	0.226	0.241	0.234	0.229	0.242	0.220	0.208

Table S3. Selected geometric parameters at critical points for HBDI$^-$ optimized at the α(0.64)-SA3-CASSCF(4,3)/6-31G* level of theory. Distances are given in Ångström and angles, dihedrals and pyramidalization in degrees with definitions provided in Figure S1.

	S_0-min	S_1-planar	S_1-I	S_1-P	MECI-I$^+$	MECI-P$^+$	S_0-min (*E*)	S_1-planar (*E*)
R_P	1.411	1.445	1.414	1.471	1.447	1.485	1.411	1.442
R_I	1.395	1.435	1.457	1.410	1.469	1.462	1.402	1.447
C-O_P	1.228	1.230	1.235	1.219	1.244	1.202	1.227	1.230
C-O_I	1.218	1.222	1.206	1.229	1.190	1.251	1.219	1.224
C_5-N_7	1.390	1.368	1.376	1.384	1.358	1.400	1.399	1.374
C_5-C_6	1.442	1.442	1.460	1.429	1.496	1.391	1.444	1.444
$\angle C_1C_4C_5$	131.5	128.1	124.8	123.5	118.0	108.3	135.1	131.9
ϕ_I	0.0	0.2	88.2	0.1	102.5	-50.3	180.0	179.5
ϕ_P	0.0	-0.2	-1.2	-89.6	-30.9	101.0	0.0	-0.2
θ_{pyr}	0.0	-0.1	0.3	-0.1	-29.6	48.3	0.0	0.1

Table S4. Selected geometric parameters at critical points for HBDI$^-$ optimized at the SA3-XMS-CASPT2(4,3)/6-31G* level of theory. Distances are given in Ångström and angles, dihedrals and pyramidalization in degrees with definitions provided in Figure S1.

	S_0-min	S_1-planar	S_1-I	S_1-P	MECI-I$^+$	MECI-P$^+$	S_0-min (*E*)	S_1-planar (*E*)
R_P	1.408	1.448	1.408	1.471	1.458	1.480	1.405	1.447
R_I	1.391	1.415	1.457	1.402	1.462	1.488	1.399	1.424
C-O_P	1.263	1.278	1.278	1.272	1.285	1.260	1.263	1.279
C-O_I	1.246	1.254	1.239	1.263	1.222	1.284	1.250	1.258
C_5-N_7	1.398	1.385	1.357	1.387	1.333	1.389	1.405	1.391
C_5-C_6	1.458	1.461	1.469	1.450	1.505	1.412	1.459	1.465
$\angle C_1C_4C_5$	132.0	127.8	122.8	121.1	114.0	103.6	135.0	132.0
ϕ_I	0.0	0.2	88.6	0.1	104.6	-36.2	180.0	179.5
ϕ_P	0.0	-0.2	-1.6	-89.6	-30.1	102.1	0.0	-0.2
θ_{pyr}	0.0	-0.2	-0.8	-0.1	-38.3	55.4	0.0	0.1

Table S5. Intersection parameters[a] for the P- and I-twisted MECIs in $HBDI^-$ as well as the approximate transition state (CI-I-TS) connecting the two minima MECI-I^+ and MECI-$I2^+$ on the I-twisted intersection seam. CI-I^+-P is similar to MECI-I^+ but with the P-torsion twisted oppositely of the pyramidalization direction.

Type	ΔE (eV)	δ_{gh} (a.u.)	Δ_{gh} (a.u.)	σ (a.u.)	θ_s (deg)	P	B
MECI-I^+	2.156	0.0400	0.4184	2.9221	5.9	6.11	3.00
MECI-$I2^+$	2.163	0.0411	0.5490	3.2166	1.2	6.69	2.49
CI-I-TS	2.234	0.0400	0.3262	3.6410	2.2	10.01	3.77
CI-I^+-P	2.288	0.0394	0.4658	2.8278	0.4	5.46	2.44
MECI-P^+	2.674	0.0429	0.4409	3.9434	6.3	11.00	3.57

[a] ΔE: energy with respect to the ground-state energy at the FC point, δ_{gh}: pitch, Δ_{gh}: asymmetry, σ, θ_s: relative tilt and tilt direction, respectively. The condition numbers P and B indicate peaked(P<1)/sloped(P>1) and bifurcating(B<1)/single-path(B>1) character. All parameters are defined in Ref. [33].

Table S6. Elements of the covalent subspace of the block effective Hamiltonian at representative geometries of $HBDI^-$ as obtained at the α(0.64)-CASSCF(4,3)/6-31G* level of theory. Energies are in kcal/mol and relative to the mean of the diagonal elements at the S_1-I geometry. The angles in parenthesis indicate displacements (in degrees) relative to the S_1-I minimum along .

Elmt.\Geom	FC	S_1-I	MECI-I^+	S_1-P	MECI-P^+	(0,106,-20) out-of-phase	(0,106,20) in-phase	no P-torsion[a]	bond+angle[b]
	-27.8	9.2	8.7	-32.6	0.2	10.3	2.3	9.9	9.7
	16.2	17.9	21.1	24.2	29.1	19.5	18.6	23.0	21.7
	-25.9	-27.0	-11.9	16.1	17.2	-23.3	-23.5	-9.3	-17.0
	18.9	30.1	26.1	0.0	-1.9	29.1	26.6	25.5	28.3
	19.7	0.0	-0.3	32.2	22.3	-0.0	5.3	1.3	0.3
	-25.2	0.4	-0.2	0.0	-1.5	0.8	-10.5	-2.1	-0.6

[a] Geometry with bonds, angles and dihedrals corresponding to MECI-I^+ but with a zero P-dihedral angle.

[b] Geometry with bonds and angles corresponding to MECI-I^+, but with dihedrals and pyramidalization adjusted to S_1-I (0,90,0).

Coordinates for critical points

Table S7. The α(0.64)-SA3-CASSCF(4,3)/6-31G* geometry of S_0 minimum. Coordinates in Ångström.

Atom	x	y	z
C	-25.7125060544	4.2253314131	-2.5465203909
N	-24.5288046439	3.7595871134	-2.4366570793
N	-26.2128482755	4.1265362025	-3.8273021081
C	-25.2361828950	3.5303446302	-4.6221161208
O	-25.3705636758	3.3016269212	-5.8107951722
C	-24.1547214283	3.3027720317	-3.6953942734
C	-21.7860726763	2.4057790020	-3.3323277736
C	-21.6089354578	2.6658385371	-1.9394681210
H	-22.4165174626	3.1291033986	-1.4059048035
C	-20.6832078511	1.7887147363	-3.9959021152
H	-20.7836789611	1.5780985933	-5.0493987622
C	-20.4637810899	2.3463810642	-1.2872692273
H	-20.3528255980	2.5520712584	-0.2362220521
C	-19.5305630054	1.4611035490	-3.3647256359
H	-18.7171064935	0.9962270806	-3.8948501278
C	-19.3322933106	1.7180026567	-1.9484475943
O	-18.2946119845	1.4279659168	-1.3598505322
C	-22.9483880251	2.7116114388	-4.0714052167
H	-22.9222242352	2.4505733784	-5.1160302844
C	-26.5034334866	4.8203626218	-1.4280290650
H	-26.7760688038	5.8530463092	-1.6337976816
H	-25.9028214100	4.7921044337	-0.5294145939
H	-27.4242474721	4.2693325469	-1.2500589818
C	-27.4967709262	4.5433457903	-4.3164214357
H	-27.5289075780	4.3018015210	-5.3681692660
H	-28.3068680365	4.0246838011	-3.8116541055
H	-27.6447689868	5.6128746976	-4.1967814484

Table S8. The α(0.64)-SA3-CASSCF(4,3)/6-31G* geometry of the S_1 planar structure. Note that this is a first-order saddle point and not a true minimum at this level of theory. Coordinates in Ångström.

Atom	x	y	z
C	-25.7022003325	4.2204507092	-2.5568518694
N	-24.5054039815	3.7393185132	-2.4898491475
N	-26.2245612336	4.1339807268	-3.8227012660
C	-25.2681287450	3.5405566143	-4.6421453248
O	-25.4200185727	3.3183675845	-5.8342995074
C	-24.1687972562	3.2998763035	-3.7410555360
C	-21.7729446897	2.3919748557	-3.3713109005
C	-21.6411574150	2.6691733206	-1.9831601841
H	-22.4648338155	3.1333317649	-1.4788321571
C	-20.6537987818	1.7753028137	-3.9975783891
H	-20.7230477864	1.5522171072	-5.0503799159
C	-20.5073403804	2.3621555174	-1.2897599717
H	-20.4319536661	2.5821817908	-0.2387523244
C	-19.5151096554	1.4611574268	-3.3260098541
H	-18.6848105407	0.9948822739	-3.8277204701
C	-19.3570708926	1.7348498046	-1.9067795702
O	-18.3297991095	1.4537185433	-1.2913712906
C	-22.9419216307	2.6897800676	-4.1663305563
H	-22.9116027368	2.4280086606	-5.2069428025
C	-26.4518771551	4.8034272751	-1.4082769416
H	-26.7287036262	5.8421293003	-1.5840498820
H	-25.8203876413	4.7604404649	-0.5313071597
H	-27.3706744112	4.2569453778	-1.1989210890
C	-27.5161138177	4.5604028076	-4.2829041411
H	-27.5710490479	4.3282808869	-5.3358164067
H	-28.3172171114	4.0408526620	-3.7651552468
H	-27.6557767919	5.6293509289	-4.1500554409

Table S9. The α(0.64)-SA3-CASSCF(4,3)/6-31G* geometry of the S_1-I minimum. Coordinates in Ångström.

Atom	x	y	z
C	-25.633137629	4.677820966	-3.276555173
N	-24.432627249	4.550615817	-3.722424130
N	-26.247365706	3.482772714	-3.019310017
C	-25.336550377	2.468392827	-3.334390610
O	-25.580972253	1.291342370	-3.239510722
C	-24.156599093	3.203904417	-3.780577957
C	-21.779474622	2.371256640	-3.417496336
C	-21.732648562	2.665698588	-2.026261128
H	-22.599155460	3.113864497	-1.569044672
C	-20.594942345	1.788288295	-3.955038747
H	-20.585563964	1.546556424	-5.006915174
C	-20.638406000	2.411158859	-1.256177949
H	-20.640066417	2.650095131	-0.205966953
C	-19.492031218	1.527951342	-3.204968204
H	-18.615403635	1.086920999	-3.649055325
C	-19.429086441	1.821977308	-1.787658930
O	-18.430655234	1.591935058	-1.098699024
C	-22.898930327	2.630444345	-4.241902005
H	-22.823854746	2.396490239	-5.291532202
C	-26.313927446	5.987093613	-3.051490945
H	-27.222476178	6.067780918	-3.643012754
H	-25.637526609	6.781447381	-3.332683476
H	-26.591766108	6.112327000	-2.008111669
C	-27.573258726	3.245897274	-2.515608966
H	-27.697721495	2.176319784	-2.441698690
H	-27.711255388	3.685356526	-1.532757570
H	-28.331582711	3.643463942	-3.183245422

Table S10. The α(0.64)-SA3-CASSCF(4,3)/6-31G* geometry of the S_1-P minimum. Coordinates in Ångström.

Atom	x	y	z
C	-25.6113207123	4.1544014972	-2.6041237208
N	-24.4294438756	3.6514673052	-2.5906135635
N	-26.1809358896	4.1173130822	-3.8523642633
C	-25.2628761356	3.5275232143	-4.7288650336
O	-25.4801383536	3.3515459479	-5.9261021101
C	-24.1479992917	3.2407632768	-3.8820394045
C	-21.8219368141	2.3563519280	-3.3860046065
C	-20.7710330447	3.3024682392	-3.1744735394
H	-20.8518377439	4.2472791629	-3.6821583112
C	-21.7077418763	1.1160868103	-2.6837550592
H	-22.4998055850	0.4009849727	-2.8186776354
C	-19.7100643093	3.0475645809	-2.3779633069
H	-18.9253795688	3.7688684890	-2.2324263172
C	-20.6611334393	0.8273495248	-1.8798800062
H	-20.5878639593	-0.1124196973	-1.3615620405
C	-19.5715745183	1.7773721320	-1.6703721291
O	-18.6149938219	1.5275434329	-0.9578945896
C	-22.9445752753	2.6334333250	-4.2946991810
H	-22.8499903014	2.3592599631	-5.3308424546
C	-26.3134981947	4.7202454832	-1.4137499868
H	-26.5708573175	5.7696289396	-1.5504545935
H	-25.6565265256	4.6365773349	-0.5582600194
H	-27.2378497575	4.1883682724	-1.1926019002
C	-27.4756238554	4.5815411744	-4.2548867373
H	-27.5673005247	4.3812872109	-5.3120819004
H	-28.2738536686	4.0641317978	-3.7279689448
H	-27.5938057246	5.6494960828	-4.0873622692

Table S11. The α(0.64)-SA3-CASSCF(4,3)/6-31G* geometry of the MECI-I^+ minimum. Coordinates in Ångström.

Atom	x	y	z
C	-25.6185205584	4.7017946199	-3.3064317261
N	-24.4126077180	4.7493536129	-3.7797265182
N	-26.1187097060	3.4456814915	-3.1673907332
C	-25.1183495705	2.5643034770	-3.5942329357
O	-25.2424039691	1.3822581922	-3.6542393512
C	-23.9919570653	3.4725529481	-3.9734780325
C	-21.7102145667	2.5898629829	-3.4625125455
C	-21.6668141461	3.0390044449	-2.1243667938
H	-22.3802482435	3.7832642945	-1.8019844197
C	-20.7075277382	1.6520224206	-3.8021159884
H	-20.6887835794	1.2724542870	-4.8136956084
C	-20.7409605234	2.5974004410	-1.2140091668
H	-20.7504265380	2.9766463079	-0.2046548748
C	-19.7636474163	1.2095663156	-2.9163919191
H	-19.0171478768	0.4974932894	-3.2298071842
C	-19.7140243217	1.6458189219	-1.5434870305
O	-18.8636606609	1.2433859805	-0.7288114459
C	-22.6591879103	3.0714456902	-4.4432648324
H	-22.6776122557	2.5750753249	-5.4002796768
C	-26.4095656665	5.9120604996	-2.9395670029
H	-27.3511932566	5.9367067973	-3.4787423728
H	-25.8325326632	6.7922442462	-3.1798973759
H	-26.6345954683	5.9105898831	-1.8776318607
C	-27.4071641840	3.0359293636	-2.6658575567
H	-27.4388109134	1.9584793789	-2.7160306848
H	-27.5464464206	3.3456225349	-1.6364169550
H	-28.2127233387	3.4407808319	-3.2684360626

Table S12. The α(0.64)-SA3-CASSCF(4,3)/6-31G* geometry of the MECI-I2$^+$ minimum. Coordinates in Ångström.

Atom	x	y	z
C	-25.6234027286	4.1457184814	-2.6352148493
N	-24.3853507845	3.7702997057	-2.6268992751
N	-26.2247056807	4.0801544179	-3.8536568378
C	-25.2617474215	3.6086353507	-4.7524917988
O	-25.4440732056	3.4558722097	-5.9179955937
C	-24.0563122078	3.3960295369	-3.8937129668
C	-22.3524630051	1.5435092217	-3.9837882912
C	-23.2499827414	0.4958726991	-3.6889458360
H	-24.3127631783	0.6915066443	-3.7107691738
C	-20.9891902494	1.1747520774	-3.9429107892
H	-20.2515800116	1.9339132232	-4.1612294961
C	-22.8447928762	-0.7787713082	-3.3830572122
H	-23.5764469283	-1.5410652765	-3.1683980514
C	-20.5601223223	-0.0916548373	-3.6465533587
H	-19.5056317979	-0.3162985933	-3.6338760780
C	-21.4618772525	-1.1699144277	-3.3373077863
O	-21.0835834161	-2.3240104424	-3.0593212496
C	-22.7504777653	2.8873537681	-4.3431419857
H	-21.9903255374	3.6518349013	-4.2965218253
C	-26.3530202690	4.6143157249	-1.4212630297
H	-26.7189539690	5.6266621032	-1.5605232098
H	-25.6803010008	4.5856780838	-0.5777049731
H	-27.2068280544	3.9752560664	-1.2214949977
C	-27.5810550279	4.4146152533	-4.2116573882
H	-27.6852983891	4.2278598002	-5.2692534550
H	-28.2930800786	3.7998122344	-3.6734768914
H	-27.7955341007	5.4591633819	-4.0154336000

Table S13. The α(0.64)-SA3-CASSCF(4,3)/6-31G* geometry of the MECI-P^+ minimum. Coordinates in Ångström.

Atom	x	y	z
C	0.3666664359	2.2620609841	0.5005272359
N	0.5435989149	1.4596108221	-0.4807538604
N	-0.1822420515	1.6247131190	1.5821276157
C	-0.3978875221	0.2712285027	1.2378127634
O	-0.9188241331	-0.5400964627	2.0350967474
C	0.0917760644	0.2023538033	-0.0626749511
C	-0.3897141645	-0.6811406748	-2.2287546940
C	0.4665960478	-0.3800352937	-3.3636263731
H	1.5182165315	-0.3523692429	-3.1598281388
C	-1.8304104021	-0.6310642173	-2.4537074813
H	-2.4482039137	-0.7738960819	-1.5888557071
C	-0.0262294050	-0.1753690765	-4.5854743444
H	0.5964682985	0.0264580389	-5.4373331976
C	-2.3499239008	-0.4568218276	-3.6671880841
H	-3.4078559772	-0.4612599970	-3.8551313345
C	-1.4807275025	-0.2275693411	-4.8407229342
O	-1.9332866017	-0.0910868869	-5.9453870259
C	0.1960009342	-0.9911468805	-0.8998591011
H	-0.3049622052	-1.8423330790	-0.4568278151
C	0.7102711341	3.7178794746	0.5018220921
H	-0.1596031200	4.3529871891	0.6717165262
H	1.1329540823	3.9722491554	-0.4622595158
H	1.4396884176	3.9719279861	1.2710484387
C	-0.5236358474	2.1698805074	2.8578387611
H	-0.9329539706	1.3571625847	3.4399564345
H	0.3431667954	2.5762025573	3.3780878846
H	-1.2680779110	2.9622566867	2.7840009791

Table S14. The α(0.64)-SA3-CASSCF(4,3)/6-31G* geometry of the S_0-*E* minimum. Coordinates in Ångström.

Atom	x	y	z
C	-25.7187887889	4.2287547800	-2.5739848134
N	-24.5459272658	3.7361944771	-2.6370732404
N	-26.3699187084	4.2038131733	-3.7866217145
C	-25.5163159450	3.6306651232	-4.7284823011
O	-25.8349357271	3.4807575596	-5.8956098759
C	-24.3314200559	3.3326603544	-3.9590302980
C	-22.5154310323	2.2351930407	-5.4623772820
C	-23.1248112188	2.1738254968	-6.7537366036
H	-24.1219120020	2.5527606443	-6.8627056592
C	-21.1858602459	1.7156544243	-5.3767710764
H	-20.6947869355	1.7458646528	-4.4164662761
C	-22.4791283561	1.6546962503	-7.8271217750
H	-22.9591360621	1.6193519253	-8.7900658009
C	-20.5245053850	1.1937542863	-6.4356312620
H	-19.5233011072	0.8111452049	-6.3350285644
C	-21.1286207403	1.1233015849	-7.7559643429
O	-20.5433373370	0.6534236698	-8.7267931291
C	-23.0971424381	2.7532031430	-4.2854540026
H	-22.4592724844	2.7013280596	-3.4187855303
C	-26.3539707357	4.7800260471	-1.3391940121
H	-26.6302844265	5.8249590418	-1.4610507029
H	-25.6477813030	4.7003812025	-0.5241059714
H	-27.2563553713	4.2338103595	-1.0733947055
C	-27.6938374330	4.6670740508	-4.0939039247
H	-27.8610055952	4.4794215708	-5.1433936936
H	-28.4476464654	4.1384001564	-3.5172126379
H	-27.8002421227	5.7317533655	-3.9055212733

Table S15. The α(0.64)-SA3-CASSCF(4,3)/6-31G* geometry of the S_1-planar-*E* structure. Note that this is not a true minimum at this level of theory. Coordinates in Ångström.

Atom	x	y	z
C	-25.7452273840	4.2405179140	-2.5788732942
N	-24.5574755947	3.7438834622	-2.6374193516
N	-26.3731422044	4.2093977383	-3.7896237775
C	-25.5017785702	3.6353608698	-4.7226655367
O	-25.8152037969	3.4866896856	-5.8963811430
C	-24.3289111055	3.3448250648	-3.9322933693
C	-22.4778425374	2.2262692608	-5.4438837399
C	-23.1209874214	2.1693453601	-6.7094947030
H	-24.1191008107	2.5500681609	-6.7931533956
C	-21.1507730499	1.7069783034	-5.3915007798
H	-20.6338349656	1.7348032673	-4.4452556144
C	-22.5034942508	1.6490382999	-7.8094604405
H	-23.0141847814	1.6185974819	-8.7564277949
C	-20.5192253685	1.1850683321	-6.4736779780
H	-19.5161950916	0.8010935452	-6.4004159775
C	-21.1578154478	1.1168956498	-7.7786853604
O	-20.5920101525	0.6451710559	-8.7638380591
C	-23.0411591394	2.7530216156	-4.2254700722
H	-22.4100167242	2.7083146279	-3.3575194562
C	-26.3817238913	4.7875810213	-1.3461711140
H	-26.6601929024	5.8336334049	-1.4622806543
H	-25.6760866666	4.7065308838	-0.5306083598
H	-27.2851476404	4.2417129771	-1.0790112915
C	-27.6942043602	4.6675213130	-4.1181778691
H	-27.8445406288	4.4764687718	-5.1694223346
H	-28.4535791236	4.1372815681	-3.5505641438
H	-27.8056206931	5.7321663818	-3.9333548069

Table S16. The SA3-XMS-CASPT2(4,3)/6-31G* geometry of S_0 minimum. Coordinates in Ångström.

Atom	x	y	z
C	-25.7258228637	4.2357783841	-2.5263264113
N	-24.5047406545	3.7562931531	-2.4086308542
N	-26.2210646359	4.1327385643	-3.8160933338
C	-25.2350734830	3.5287815052	-4.6268930934
O	-25.3779159367	3.2969585673	-5.8432248426
C	-24.1478357193	3.3030276953	-3.6823958066
C	-21.7842455534	2.4043361489	-3.3351075460
C	-21.6152444088	2.6690013366	-1.9373095380
H	-22.4376918928	3.1384612631	-1.4037743020
C	-20.6866328583	1.7866130349	-4.0104204691
H	-20.7936922724	1.5756795555	-5.0765329205
C	-20.4525506506	2.3418473361	-1.2868739776
H	-20.3339142262	2.5473188466	-0.2235863411
C	-19.5195994783	1.4559462198	-3.3670853880
H	-18.6955769134	0.9855526811	-3.9018333467
C	-19.3215997431	1.7127200548	-1.9519822986
O	-18.2545473532	1.4149136056	-1.3449576098
C	-22.9478205619	2.7129809403	-4.0646314595
H	-22.9314561601	2.4519572633	-5.1261365754
C	-26.5206043111	4.8304469189	-1.4150980861
H	-26.7958427801	5.8727714602	-1.6175860543
H	-25.9079672162	4.7984187497	-0.5122577345
H	-27.4490578974	4.2762179406	-1.2304037956
C	-27.5027352778	4.5432905554	-4.3276181032
H	-27.4956516177	4.2831131577	-5.3886679665
H	-28.3248065330	4.0175876326	-3.8300250045
H	-27.6560288253	5.6224680728	-4.2194611103

Table S17. The SA3-XMS-CASPT2(4,3)/6-31G* geometry of the S_1 planar structure. Coordinates in Ångström.

Atom	x	y	z
C	-25.7098856841	4.2289361254	-2.5352517605
N	-24.4717568765	3.7323026652	-2.4605011975
N	-26.2287695741	4.1386993696	-3.8108857333
C	-25.2676642461	3.5389301835	-4.6483831239
O	-25.4269376934	3.3125643458	-5.8710230411
C	-24.1533071417	3.2947016211	-3.7355749735
C	-21.7726284460	2.3893712127	-3.3814227629
C	-21.6582329822	2.6755664417	-1.9866691878
H	-22.5025511537	3.1465639916	-1.4899940928
C	-20.6598502600	1.7731580441	-4.0165707258
H	-20.7295021287	1.5469459905	-5.0826999679
C	-20.5025399572	2.3606033602	-1.2885001116
H	-20.4228435725	2.5821806755	-0.2239401780
C	-19.5033095369	1.4574449990	-3.3207045973
H	-18.6581459130	0.9851981632	-3.8212949151
C	-19.3584956938	1.7351925163	-1.9081553953
O	-18.2925143283	1.4441215856	-1.2670439920
C	-22.9489484961	2.6917658611	-4.1700681334
H	-22.9284783259	2.4297121384	-5.2282229956
C	-26.4615907804	4.8109452315	-1.3924476785
H	-26.7413040305	5.8606966453	-1.5600841185
H	-25.8145666719	4.7622131306	-0.5135000859
H	-27.3883290277	4.2623643867	-1.1714599871
C	-27.5196671726	4.5600712810	-4.2912940382
H	-27.5375484480	4.3099735823	-5.3549147470
H	-28.3327462925	4.0338349496	-3.7793342800
H	-27.6641863910	5.6390556045	-4.1683755250

Table S18. The SA3-XMS-CASPT2(4,3)/6-31G* geometry of the S_1-I minimum. Coordinates in Ångström.

Atom	x	y	z
C	-25.6335663362	4.6873324011	-3.2769572790
N	-24.3937534807	4.5513422441	-3.7915816979
N	-26.2217721056	3.4882077453	-3.0152175676
C	-25.3036043124	2.4682734328	-3.3806367893
O	-25.5503394531	1.2570955665	-3.2912287038
C	-24.1381657099	3.2203740000	-3.8632008968
C	-21.7985950043	2.3806678411	-3.4824213353
C	-21.8028151018	2.7042602114	-2.0891381860
H	-22.6895738048	3.1808948159	-1.6661009852
C	-20.5999060860	1.7746343463	-3.9712148107
H	-20.5528057283	1.5105437964	-5.0305801260
C	-20.7182428966	2.4471773547	-1.2740231719
H	-20.7544330252	2.7090678818	-0.2158794353
C	-19.5155110541	1.5187030359	-3.1552770899
H	-18.6169736622	1.0556188848	-3.5648666697
C	-19.4977414738	1.8349106984	-1.7463999721
O	-18.4962001074	1.5991588381	-0.9887472324
C	-22.8914935704	2.6317895935	-4.3334283813
H	-22.8260860789	2.3643322793	-5.3896791840
C	-26.2904829396	5.9951181484	-3.0117055559
H	-27.2296123038	6.0998152436	-3.5680668541
H	-25.6041126000	6.7843340760	-3.3213726395
H	-26.5210197289	6.1241444309	-1.9475939345
C	-27.5257276189	3.2148462429	-2.4588039997
H	-27.6077413217	2.1272451819	-2.4067360385
H	-27.6249919042	3.6366785011	-1.4545408941
H	-28.3217185289	3.6106064794	-3.0966953182

Table S19. The SA3-XMS-CASPT2(4,3)/6-31G* geometry of the S_1-P minimum. Coordinates in Ångström.

Atom	x	y	z
C	-25.5903787063	4.1489900005	-2.5892936586
N	-24.3619230340	3.6207873565	-2.5990909489
N	-26.1696784720	4.1153083780	-3.8401464154
C	-25.2629850359	3.5221537799	-4.7532435524
O	-25.5090960583	3.3518687249	-5.9799224618
C	-24.1238627741	3.2248535908	-3.9072823047
C	-21.8309852481	2.3549842577	-3.4097475299
C	-20.8103648035	3.3112535437	-3.1990159963
H	-20.8877998780	4.2617090092	-3.7218877333
C	-21.7453362984	1.1292195039	-2.7092324994
H	-22.5413236037	0.4027727558	-2.8556640651
C	-19.7401944790	3.0577086397	-2.3573459325
H	-18.9502316607	3.7885866559	-2.1975236315
C	-20.6863206881	0.8495827506	-1.8617446952
H	-20.6140853718	-0.0945985854	-1.3259569409
C	-19.6277486039	1.8052593460	-1.6529245746
O	-18.6428832007	1.5551209680	-0.8872613282
C	-22.9366841857	2.6193312087	-4.3429339185
H	-22.8374724996	2.3403872543	-5.3911285435
C	-26.2725573357	4.7077867251	-1.3906913756
H	-26.5316717840	5.7708065737	-1.5019422420
H	-25.5861424449	4.6093030466	-0.5460313142
H	-27.2033183057	4.1775303506	-1.1412659373
C	-27.4665166153	4.5792201767	-4.2476761119
H	-27.5300230793	4.3638746100	-5.3176834259
H	-28.2736795268	4.0553789566	-3.7211003660
H	-27.5866963911	5.6572539053	-4.0844461204

Table S20. The SA3-XMS-CASPT2(4,3)/6-31G* geometry of the MECI-I^+ minimum. Coordinates in Ångström.

Atom	x	y	z
C	-25.6099470789	4.7068517234	-3.3180351026
N	-24.3675076654	4.7612007685	-3.8814319381
N	-26.0672535430	3.4469828966	-3.1666789911
C	-25.0534529349	2.5797082585	-3.6516889622
O	-25.1787308118	1.3673466786	-3.7409204556
C	-23.9515806007	3.5103399726	-4.0814025826
C	-21.7385422439	2.6160537234	-3.5363984933
C	-21.7604630194	3.0794782359	-2.1985393014
H	-22.4814019627	3.8508743448	-1.9096630184
C	-20.7248304374	1.6690848486	-3.8234470355
H	-20.6557562941	1.2749961700	-4.8420546797
C	-20.8683419693	2.6213989130	-1.2327593595
H	-20.9298380149	3.0128091868	-0.2148390481
C	-19.8240148582	1.2203231020	-2.8639306711
H	-19.0630896919	0.4875148317	-3.1415297874
C	-19.8339419086	1.6544435450	-1.4911922632
O	-19.0126518965	1.2310519841	-0.5978000015
C	-22.6340196085	3.1131739440	-4.5742944746
H	-22.7142530044	2.4913111604	-5.4706085056
C	-26.3660846655	5.9101796993	-2.8858577298
H	-27.3541071501	5.9472345168	-3.3549248117
H	-25.7932550425	6.7914924301	-3.1718115954
H	-26.5073337770	5.9110243283	-1.8004957564
C	-27.3176203150	2.9868413911	-2.5966426543
H	-27.3029161551	1.8984448719	-2.6717326107
H	-27.3966572866	3.2802462916	-1.5480569593
H	-28.1682443393	3.3813907616	-3.1567238656

Table S21. The SA3-XMS-CASPT2(4,3)/6-31G* geometry of the MECI-I2$^+$ minimum. Coordinates in Ångström.

Atom	x	y	z
C	-25.5917874478	4.1573060543	-2.6654492956
N	-24.2842587567	3.7743005189	-2.6585372720
N	-26.1536426362	4.1051468516	-3.8892094278
C	-25.1436515676	3.6591849476	-4.7812519492
O	-25.3047720417	3.5349229730	-5.9877403014
C	-23.9469852297	3.4406983443	-3.9064930848
C	-22.3441254374	1.5647749265	-3.9663953875
C	-23.3193460621	0.5575832248	-3.7672649231
H	-24.3818358529	0.7993081353	-3.8838172948
C	-21.0057735138	1.1287245421	-3.8162951702
H	-20.2032353982	1.8598587638	-3.9568290556
C	-22.9899957368	-0.7516432605	-3.4281549835
H	-23.7862743343	-1.4854773557	-3.2826681186
C	-20.6723670919	-0.1826321298	-3.4883324365
H	-19.6203954181	-0.4577747134	-3.3817195688
C	-21.6393215817	-1.2235180761	-3.2649068097
O	-21.3392092373	-2.4350675618	-2.9526188893
C	-22.6577147201	2.9261518360	-4.3782294815
H	-21.8734173886	3.6695239563	-4.2090228354
C	-26.3249937283	4.5862895571	-1.4464288404
H	-26.7115316478	5.6042956025	-1.5563720542
H	-25.6351443158	4.5462439035	-0.6045433763
H	-27.1717075287	3.9217811189	-1.2504971264
C	-27.5112102881	4.4154202314	-4.2909050698
H	-27.5575688031	4.2409823023	-5.3671009482
H	-28.2227849229	3.7616670848	-3.7827713026
H	-27.7503644552	5.4597399469	-4.0782943457

Table S22. The SA3-XMS-CASPT2(4,3)/6-31G* geometry of the MECI-P^+ minimum. Coordinates in Ångström.

Atom	x	y	z
C	0.1875043105	2.2218069520	0.4135663993
N	0.3097490002	1.3266905995	-0.5794672068
N	-0.1477014627	1.5872089154	1.5819531501
C	-0.3041657467	0.1771660125	1.3489028636
O	-0.6718280869	-0.6292709489	2.2779258190
C	0.0320734598	0.0858086251	-0.0196838069
C	-0.4100462178	-0.6838887526	-2.1758259746
C	0.5103191255	-0.4336950676	-3.2236439716
H	1.5604664290	-0.5337736796	-2.9852887826
C	-1.8018828699	-0.4521912231	-2.4191005677
H	-2.4682170458	-0.5373122779	-1.5697004787
C	0.0744203190	-0.1711290609	-4.5025788735
H	0.7482031058	-0.0264401830	-5.3412757359
C	-2.2758119059	-0.2482375480	-3.6883840290
H	-3.3326819225	-0.1727128631	-3.9257188551
C	-1.3420739398	-0.0898910732	-4.7803793030
O	-1.7470166452	0.1018683119	-5.9576990517
C	0.0924432369	-1.1400729576	-0.8601306469
H	-0.5996068364	-1.8995111980	-0.4682584807
C	0.4712193848	3.6802411616	0.3067827965
H	-0.3722516119	4.3146406169	0.6212717715
H	0.6845026793	3.9010561018	-0.7438863045
H	1.3422622449	4.0041874132	0.8984543440
C	-0.3738405820	2.1441447358	2.8812183233
H	-0.6230136276	1.2834160006	3.5104336856
H	0.5161061406	2.6519465022	3.2796226408
H	-1.2082659065	2.8607272344	2.8925411956

Table S23. The SA3-XMS-CASPT2(4,3)/6-31G* geometry of the S_0-*E* minimum. Coordinates in Ångström.

Atom	x	y	z
C	-25.7247295599	4.2360372726	-2.5545701885
N	-24.5141370315	3.7283892066	-2.6158741314
N	-26.3690788371	4.2055628698	-3.7787656032
C	-25.5080767969	3.6256153866	-4.7360282324
O	-25.8406430048	3.4745310830	-5.9316438340
C	-24.3169598637	3.3294191291	-3.9481451484
C	-22.5114711417	2.2362183422	-5.4511730986
C	-23.1412935193	2.1842218979	-6.7384110962
H	-24.1521012034	2.5723061145	-6.8326064132
C	-21.1792506497	1.7155494552	-5.3657642042
H	-20.6794745660	1.7445727298	-4.3954348939
C	-22.4889723625	1.6591229172	-7.8252561240
H	-22.9775554088	1.6249124973	-8.7981858358
C	-20.5230055630	1.1899638859	-6.4487912157
H	-19.5101005321	0.7999162143	-6.3592914340
C	-21.1383115605	1.1255949919	-7.7627871445
O	-20.5456186035	0.6442968434	-8.7688891940
C	-23.0859498721	2.7508212846	-4.2763664830
H	-22.4394697973	2.6984963303	-3.3967119312
C	-26.3665810308	4.7876903290	-1.3280082806
H	-26.6456252938	5.8420555972	-1.4464851551
H	-25.6492638766	4.7049041898	-0.5092562711
H	-27.2760583774	4.2380234838	-1.0549348669
C	-27.6933726436	4.6628063445	-4.1111530490
H	-27.8206276994	4.4552675129	-5.1759187243
H	-28.4609442860	4.1279519717	-3.5411938264
H	-27.8070022075	5.7379257643	-3.9338340899

Table S24. The SA3-XMS-CASPT2(4,3)/6-31G* geometry of the S_1-planar-*E* structure. Note that this is not a true minimum at this level of theory. Coordinates in Ångström.

Atom	x	y	z
C	-25.7521906773	4.2490319272	-2.5571810297
N	-24.5245667920	3.7387920271	-2.6043102926
N	-26.3702206112	4.2103958515	-3.7793423949
C	-25.4886706709	3.6282401692	-4.7268181998
O	-25.8183865847	3.4782303386	-5.9312659006
C	-24.3023262383	3.3371489200	-3.9176616039
C	-22.4715186142	2.2263298213	-5.4322585643
C	-23.1385438730	2.1814207248	-6.6910572798
H	-24.1517821928	2.5729709706	-6.7578390597
C	-21.1461749958	1.7073730409	-5.3792941442
H	-20.6166689379	1.7316019982	-4.4242471627
C	-22.5110845247	1.6530165084	-7.8106138314
H	-23.0322437791	1.6249820402	-8.7678935772
C	-20.5186968810	1.1790201175	-6.4962893735
H	-19.5034661071	0.7868231943	-6.4350028158
C	-21.1700673644	1.1210231629	-7.7850955397
O	-20.5939698430	0.6339611835	-8.8175991002
C	-23.0358099416	2.7543135562	-4.2086838561
H	-22.3922144373	2.7068202070	-3.3294157441
C	-26.3998508749	4.7983645679	-1.3350295665
H	-26.6811592487	5.8537807915	-1.4498376384
H	-25.6848260903	4.7159979052	-0.5137080261
H	-27.3107353233	4.2487889565	-1.0615813908
C	-27.6912594526	4.6611120068	-4.1371231881
H	-27.7975015366	4.4478544482	-5.2032091358
H	-28.4651260368	4.1242851621	-3.5775907928
H	-27.8104126736	5.7365564194	-3.9656812090

References

1. J. W. Snyder, Jr., B. S. Fales, E. G. Hohenstein, B. G. Levine and T. J. Martinez, *J. Chem. Phys.*, 2017, **146**, 174113.
2. H. Jónsson, G. Mills and K. W. Jacobsen, in *Classical and Quantum Dynamics in Condensed Phase Simulations*, eds. B. J. Berne, G. Ciccotti and D. F. Coker, World Scientific, 1998, DOI: 10.1142/9789812839664_0016, pp. 385-404.
3. A. V. Bochenkova and L. H. Andersen, *Faraday Discuss.*, 2013, **163**, 297-319.
4. J. Kastner, J. M. Carr, T. W. Keal, W. Thiel, A. Wander and P. Sherwood, *J. Phys. Chem. A*, 2009, **113**, 11856-11865.
5. C. Aldaz, J. A. Kammeraad and P. M. Zimmerman, *Phys. Chem. Chem. Phys.*, 2018, **20**, 27394-27405.
6. C. Aldaz, pyGSM, https://github.com/ZimmermanGroup/pyGSM/, 2020).
7. T. Shiozaki, *WIREs Comp. Mol. Sci.*, 2017, **8**, e1331.
8. C. Chen, L. Zhu, M. S. Baranov, L. Tang, N. S. Baleeva, A. Y. Smirnov, I. V. Yampolsky, K. M. Solntsev and C. Fang, *The Journal of Physical Chemistry B*, 2019, **123**, 3804-3821.
9. S. Olsen and R. H. McKenzie, *J. Chem. Phys.*, 2009, **130**, 184302.
10. M. G. Romei, C.-Y. Lin, I. I. Mathews and S. G. Boxer, *Science*, 2020, **367**, 76-79.
11. S. F. Boys, *Rev. Mod. Phys.*, 1960, **32**, 296-299.
12. T. Pacher, L. S. Cederbaum and H. Köppel, *J. Chem. Phys.*, 1988, **89**, 7367-7381.
13. L. S. Cederbaum, J. Schirmer and H. D. Meyer, *J. Phys. A: Math. Gen.*, 1989, **22**, 2427-2439.
14. R. McWeeny and C. A. Coulson, *Proc. R. Soc. London, Ser. A*, 1954, **223**, 306-323.
15. P. J. K. H.-J. Werner, G. Knizia, F. R. Manby, M. Schütz, P. Celani, W. Györffy, D. Kats, T. Korona, R. Lindh, A. Mitrushenkov, G. Rauhut, K. R. Shamasundar, T. B. Adler, R. D. Amos, A. Bernhardsson, A. Berning, D. L.Cooper, M. J. O. Deegan, A. J. Dobbyn, F. Eckert, E. Goll, C. Hampel, A. Hesselmann, G. Het-zer, T. Hrenar, G. Jansen, C. Köppl, Y. Liu, A. W. Lloyd, R. A. Mata, A. J. May, S. J. McNi-cholas, W. Meyer, M. E. Mura, A. Nicklass, D. P. O'Neill, P. Palmieri, D. Peng, K. Pflüger,R. Pitzer, M. Reiher, T. Shiozaki, H. Stoll, A. J. Stone, R. Tarroni, T. Thorsteinsson, and M. Wang, MOLPRO, version 2015.1, a package of ab initio programs, see http://www.molpro.net.).
16. H.-J. Werner, P. J. Knowles, G. Knizia, F. R. Manby and M. Schütz, *WIREs Computational Molecular Science*, 2012, **2**, 242-253.
17. A. M. D. Lee, J. D. Coe, S. Ullrich, M. L. Ho, S. J. Lee, B. M. Cheng, M. Z. Zgierski, I. C. Chen, T. J. Martinez and A. Stolow, *The Journal of Physical Chemistry A*, 2007, **111**, 11948-11960.
18. M. S. Schuurman and A. Stolow, *Annu. Rev. Phys. Chem.*, 2018, **69**, 427-450.
19. J. P. Malhado and J. T. Hynes, *J. Chem. Phys.*, 2016, **145**, 194104.
20. B. G. Levine and T. J. Martinez, *Ann. Rev. Phys. Chem.*, 2007, **58**, 613-634.
21. M. Ben-Nun, F. Molnar, K. Schulten and T. J. Martinez, *Proc. Natl. Acad. Sci.*, 2002, **99**, 1769-1773.
22. M. Araújo, B. Lasorne, A. L. Magalhães, M. J. Bearpark and M. A. Robb, *The Journal of Physical Chemistry A*, 2010, **114**, 12016-12020.

23. C. Schnedermann, X. Yang, M. Liebel, K. M. Spillane, J. Lugtenburg, I. Fernández, A. Valentini, I. Schapiro, M. Olivucci, P. Kukura and R. A. Mathies, *Nat. Chem.*, 2018, **10**, 449-455.
24. C. A. Farfan and D. B. Turner, *Phys. Chem. Chem. Phys.*, 2020, **22**, 20265-20283.
25. G. J. Atchity, S. S. Xantheas and K. Ruedenberg, *The Journal of Chemical Physics*, 1991, **95**, 1862-1876.
26. D. R. Yarkony, *J. Chem. Phys.*, 2001, **114**, 2601-2613.
27. S. Matsika and P. Krause, *Ann. Rev. Phys. Chem.*, 2011, **62**, 621-643.
28. A. M. Virshup, J. Chen and T. J. Martinez, *J. Chem. Phys.*, 2012, **137**, 22A519.
29. M. A. Robb, F. Bernardi and M. Olivucci, *Pure Appl. Chem.*, 1995, **67**, 783-789.
30. W. Fuß, S. Lochbrunner, A. M. Müller, T. Schikarski, W. E. Schmid and S. A. Trushin, *Chem. Phys.*, 1998, **232**, 161-174.
31. M. A. Robb, M. Garavelli, M. Olivucci and F. Bernardi, in *Rev. Comput. Chem.*, 2000, DOI: https://doi.org/10.1002/9780470125922.ch2, pp. 87-146.
32. I. Schapiro, M. N. Ryazantsev, L. M. Frutos, N. Ferré, R. Lindh and M. Olivucci, *JACS*, 2011, **133**, 3354-3364.
33. I. Fdez. Galván, M. l. G. Delcey, T. B. Pedersen, F. Aquilante and R. Lindh, *J. Chem. Theory Comput.*, 2016, **12**, 3636-3653.
34. B. Sellner, M. Barbatti and H. Lischka, *J. Chem. Phys.*, 2009, **131**, 024312.
35. D. R. Yarkony, *J. Chem. Phys.*, 2000, **112**, 2111-2120.
36. S. B. Nielsen, A. Lapierre, J. U. Andersen, U. Pedersen, S. Tomita and L. Andersen, *Phys. Rev. Lett.*, 2001, **87**, 228102.
37. C. R. S. Mooney, D. A. Horke, A. S. Chatterley, A. Simperler, H. H. Fielding and J. R. R. Verlet, *Chem. Sci.*, 2013, **4**, 921-927.
38. J. R. Verlet, personal communication.
39. M. D. Davari, F. J. Ferrer, D. Morozov, F. Santoro and G. Groenhof, *Chemphyschem*, 2014, **15**, 3236-3245.
40. G. Henkelman, B. P. Uberuaga and H. Jónsson, *J. Chem. Phys.*, 2000, **113**, 9901-9904.
41. J. D. Coe, B. G. Levine and T. J. Martínez, *J. Phys. Chem. A*, 2007, **111**, 11302-11310.
42. V. N. Staroverov and E. R. Davidson, *JACS*, 2000, **122**, 186-187.
43. J. Conyard, I. A. Heisler, Y. Chan, P. C. Bulman Page, S. R. Meech and L. Blancafort, *Chem. Sci.*, 2018, **9**, 1803-1812.